Dissertation

submitted to the

Combined Faculty of Natural Sciences and Mathematics

of the Ruperto-Carola University Heidelberg, Germany

for the degree of

Doctor of Natural Sciences

Presented by

M.Sci Fereydoon Taheri

born in: Tehran, Iran

Oral examination: November 6, 2019

Analysis of space-time correlations of diffusive particles in viscoelastic media

To the memory of Jörg who always wanted to order the chaos

Acknowledgements

Commencing a PhD in an interdisciplinary subject with a little classical education in biology was not an easy task. It wouldn't have been possible if Prof. Jörg Langowski hadn't believed in me. I would like to start by thanking him for confiding in me and giving me the opportunity to explore, fail and learn in his lab. His memories will always stay with us. My gratitude equally extends to Dr. Katalin Tóth who always trusted me in my work, supported me in the most difficult times and never doubted my morals and my abilities. I am deeply grateful to my PhD advisor, PD Dr. Christoph Garbe for his ready help, insightful feedback and input on my progress throughout the last four and a half years. I would also like to specially thank Prof. Ralf Metzler without whose support I wouldn't have been able to finish my doctoral studies. He provided the friendliest atmosphere in Potsdam and the most considerate guidance during the last year. I am also thankful to Prof. Dr. Ulrich Schwarz and Prof. Dr. Peter Bastian for agreeing to be on my defense committee.

I am very thankful to Dr. Jaeoh Shin who generously allowed me to modify his code and Dr. Andrey Cherstvy who was there to share his knowledge at any time and place. Without their considerate help, an important part of this thesis wouldn't have been possible. Special thanks go to our esteemed collaborators, Dr. Giberto Chirico who was always available to comment and discuss problems, Giulia Marcarini whose persistence pushed the project to its current state and Dr. György Vámosi for all the fruitful discussions and insights.

I would like to thank the members of B040 over the years. Thanks to Jan for all his help at the start of my PhD, Tabea for her selfless contributions, Alex for all his mentoring, Kathrin for her kindness and assistance whenever it was needed, Ruihan for teaching me how to be more organised (sorry I failed you!) and her pure comradeship and finally to Lukas for his unforgettable puns and the time in and out of the lab. I also would like to thank Christine and Gabi for their assistance and friendship throughout these years.

I am also very grateful to the German Cancer Research Center (dkfz.) graduate school and Heidelberg graduate school of mathematical and computational methods for the sciences (HGS MathComp) for their unequivocal support in the course of this PhD amidst all the hardships.

A special shout-out to the Potsdam gang, Samudrajit, Vittoria, Yousof and Amin for the great time we shared in Potsdam and Venice. I would like to thank my friends from HGS Mathcomp, Asha and Diego for their true friendship.

No matter how prepared I thought I was, moving away from home always leaves its scars. It would have been impossible to cope with it without my big fat Greek family here; especially Rula, Konstantina, Liolios and Sachpekedis. Thank you guys for accepting an ancient enemy in your cosy community and for all Alexander-filled conversations. It also wouldn't have been possible without unconditional emotional support of my dear friends Yasamin and Babak. Thank you for the late night meetings in the ugly basement of Bibliothek and for bringing a piece of Tehran to Heidelberg. A huge thank you also goes to Tobi for literally being a buddy and sorry for all the late requests. Finally thank you Shirin for always being there to listen and calm me down.

Last but not least, Christos and Azer... Guys I have no idea how to even start. You were the first people I met in this little city and left such a lasting mark on me that I cannot imagine a life without you. we have been through everything together. Christos, my friend, you indeed redefined friendship. Thank you for all the movie nights, discussions, arguments and laughters. And Azer, thank you for giving me the strength to always "trudge through another fortnight quite respectably". Your honest and pure "Dousti" means a lot to me.

I would like to finally express my highest appreciation and deepest love to my family. Without them, nothing would be possible. Babak, my brother, my oldest friend, it is the most difficult thing in the world to be far from you. I miss you every single day. Maman, I learnt how to be alive, and rational in this irrational world from you. Thank you for everything. And finally, Baba, I miss you...

Abstract

Diffusion is the major short-range transport mechanism in living cells. Within individual compartments of a eukaryotic cell, such as the nucleus, mitochondria or the cytosol, biological macromolecules find their targets mostly by thermally driven random motion. For instance, specific access of DNA-binding proteins to their target sequences in the genome occurs through a sequence of three-dimensional diffusion, DNA-binding and one-dimensional search events on the DNA. The DNA/chromatin network in the cell nucleus thus has two effects on protein diffusion: obstruction due to crowding and accelerated association to specific sequences through guided diffusion along the DNA chain. The problem of target finding of proteins in the cell nucleus is only one example of diffusion-controlled reactions in a dense polymer network. Outside the direct relevance for molecular and cellular biology, the study of diffusing particles in viscoelastic media has important applications in many fields of physics. By recording fast image series of two-dimensional sections of live cells, we monitor these diffusion processes in real time and gain better understanding of the underlying physics. The method used is light sheet fluorescence microscopy followed by auto (-cross) correlation analysis. We particularly studied the random motion of chromatin and its interconnection with nucleoplasmic A-type lamins. Utilizing this method, we find that

1. Nucleoplasmic lamin As and chromatin show significant co-mobility, indicating that their motions are interconnected in the nucleus.
2. The random motion of histones H2A within the chromatin network is subdiffusive, *i.e.* the effective diffusion coefficient decreases for slow timescales. Knocking out lamin A changes the diffusion back to normal. Thus, lamin A influences the dynamics of the entire chromatin network.
3. A-type lamins affect the spatial organisation of chromatin inside the cellular interior

We have also attempted to develop a modelling framework that describes chromatin dynamics within the cell nucleus in the presence and absence of nucleoplasmic A-type lamins. Our conclusion is that lamin A plays a central role in determining the viscoelasticity of the chromatin network and helping to maintain local ordering of interphase chromosomes. These findings enabled us to derive a qualitative description of diffusion based on the viscoelasticity of the cellular environment.

Zusammenfassung

Diffusion ist der wichtigste kurzstreckige Transportmechanismus in lebenden Zellen. In einzelnen Kompartimenten einer eukaryotischen Zelle, wie dem Kern, den Mitochondrien oder dem Zytosol, finden biologische Makromoleküle ihre Ziele meist durch thermisch angetriebene Zufallsbewegung. Zum Beispiel erfolgt der spezifische Zugriff von DNA-bindenden Proteinen an ihre Zielsequenzen im Genom durch eine Abfolge von dreidimensionaler Diffusion, DNA-Bindung und eindimensionaler Suche auf der DNA. Das Problem der Zielfindung von Proteinen im Zellkern ist nur ein Beispiel für diffusionskontrollierte Reaktionen in einem dichten Polymernetzwerk. Außerhalb der Relevanz für die Molekular- und Zellbiologie hat die Untersuchung von diffundierenden Partikeln in viskoelastischen Medien wichtige Anwendungen in vielen Bereichen der Physik.

Indem wir schnelle Bildserien von zweidimensionalen Abschnitten lebender Zellen aufzeichnen, können wir diese Diffusionsprozesse in Echtzeit überwachen und gewinnen ein besseres Verständnis der ihnen zugrunde liegenden Physik. Die hier verwendete Methode ist die Lichtscheiben-Fluoreszenzmikroskopie, gefolgt von einer Auto- (Kreuz-) Korrelationsanalyse. Wir untersuchten insbesondere die zufällige Bewegung von Chromatin und dessen Verknüpfung mit nukleoplasmatischen Typ A Laminen. Mithilfe dieser Methode fanden wir, dass:

1. Nucleoplasmische Typ A Lamine und Chromatin zeigten signifikante Co-Mobilität, was darauf hinweist, dass ihre Bewegungen im Kern miteinander verbunden sind.
2. Die ungeordnete Bewegung der H2A Histone innerhalb des Chromatin-Netzwerks ist subdiffusiv. Durch Ausschalten des Lamin A Gens wird die Diffusion wieder normalisiert. Somit beeinflusst Lamin A die Dynamik des gesamten Chromatin-Netzwerks.
3. Typ A Lamine beeinflussen die räumliche Organisation des Chromatins im Zellinneren.

Zusätzlich haben wir angestrebt, ein Modell-Framework zu entwickeln, das die Chromatindynamik innerhalb des Zellkerns in Gegenwart und in Abwesenheit von nukleoplasmatischen Typ A Laminen beschreibt. In diesen Modellierungen zeigte sich, dass Lamin A eine zentrale Rolle bei der Bestimmung der Viskoelastizität des Chromatin-Netzwerks spielt und dabei hilft, die lokale Anordnung der Interphasen-Chromosomen aufrechtzuerhalten. Diese Ergebnisse ermöglichten es uns, eine qualitative Beschreibung der Diffusion auf der Grundlage der Viskoelastizität der zellulären Umgebung abzuleiten.

Detailed Contents

Figures

INTRODUCTION

1 Introduction

The mystery of random motion of particles has been one of the central focuses of natural and exact scientists since the early 19th century. First observed by Dutch physician, Jan Ingenhausz, while studying the movement of finely ground carbon particles in uncovered alcohol around 1785 [1], it was Robert Brown * , a Scottish botanist, who systematically reported a jittery irregular motion of pollen that fell in dew drops [2]. In his account, he found that inorganic grains also demonstrated the same kind of movements in suspension, disputing the prevalent idea at the time, which presumed a living origin of the motions. This "peculiar" character in the motion of particles in suspension, as Brown called it, held the key to many great advancements in modern condensed matter physics *i.e.* the confirmation of the molecular nature of matter; the demonstration of the importance of thermal forces; and ultimately the acceptance of statistical physics as a valid alternative to the conventional 'world-view' at the time [3]. To understand the context, it is important to realise that many physical scientists of this pivotal period did not assume the discontinuity of the matter which is beneath the visible reality. Therefore, the very existence of molecules, ions and atoms was a subject of debate [4].

1.1 The story of a belated theory

It was not until the first decade of the 20th century that a robust mathematical description of this irregular, seemingly inexhaustible motion was proposed. In his landmark paper entitled "On the motion of small particles suspended in liquids at rest" from 1905 [5], Albert Einstein proposed a new way to quantify and describe "Brownian molecular motion", a name also coined by him †. He assumed an equilibrium between an imaginary force imposed on a particle in the form of a small sphere and the force of osmotic pressure due to the diffusive current of particles. Therefore, he derived an expression for the so-called diffusion coefficient of the suspended particles which, except for universal constants and the absolute temperature, solely depends on the physical properties of the solvent (viscosity) and on the size of the particles(equation 1.1).

$$D = \frac{RT}{N} \cdot \frac{1}{6\pi\eta_{visc}a} = \frac{k_BT}{6\pi\eta_{visc}a}, \tag{1.1}$$

Where, according to the notations he used in [5], R is the universal gas constant, T is the absolute temperature, N is the Avogadro's number, η_{visc} is the viscosity coefficient of the solvent, a is the radius of the spheres and $k_B = \frac{R}{N}$ is Boltzman's constant.

The difficulty then was to find a quantity that could describe the disordered motion of the particle in terms of its diffusion coefficient. There had been many failed attempts to quantify this motion by considering the average velocities of the particles in experiments. Einstein, though, appealed to a probabilistic description of the diffusive motion by considering the mean squared displacements of particles in a given time. He solved the celebrated Fick's diffusion equation with D as the constant coefficient ($\frac{\partial f(x,t)}{\partial t} = D\nabla^2 f(x,t)$ for $f(x,t)$ as the density of particles at position x at time t, assuming $f(-x,t) = f(x,t)$ and $\langle x \rangle = 0$). As a result he showed that the mean squared displacement of particles ($\langle x^2(t) \rangle$) moving in a d-dimensional space is growing linearly in time based on the equation 1.2 [6]:

$$\overline{x^2} = \langle x^2(t) \rangle = \int x^2(t)f(x,t)dx = 2dDt, \tag{1.2}$$

---

* Adolphe-Thédore Brongniart had published similar observations in his memoir one year prior Brown. Brown mentioned his work and made some critical comments about it in his letter
† Reportedly Einstein did not have access to Brown's original work. [1]

It is worth mentioning that an equivalent description of random motion was presented in the doctoral thesis of the French mathematician, Louis Bachelier [7] in 1900, five years prior Einstein studies. He applied the same approach, which later became known as the theory of random walks *, to explain the fluctuation of stock prices. However, Einstein seemed not to be aware of Bachelier's studies.

The publication of Einstein's results, and later independent works of Marian Smoluchowski and Paul Langevin, paved the way for further developments in the theory of stochastic motion in next decades. On the other hand, before their theoretical works, experimentalists were quite confused in treating Brownian motion. They simply did not know what to measure. But after 1905, the theory provided a clear clue for precise and meaningful measurements. Especially after Paul Langevin called for more controlled measurements with grains of known size, Jean Baptiste Perrin, a French experimental physicist and Langevin's close friend, designed a series of clever experiments to follow motion trajectories of small suspended putty particles and he managed to estimate Avogadro's number with surprising accuracy(70.5×10^{22}). More importantly, these simple reproducible experiments provided a firm observational ground for the theorists' predictions and consequently settled a century long dispute, against "the ambient scepticism" [8], between high profile scientists over the existence of atoms[†].
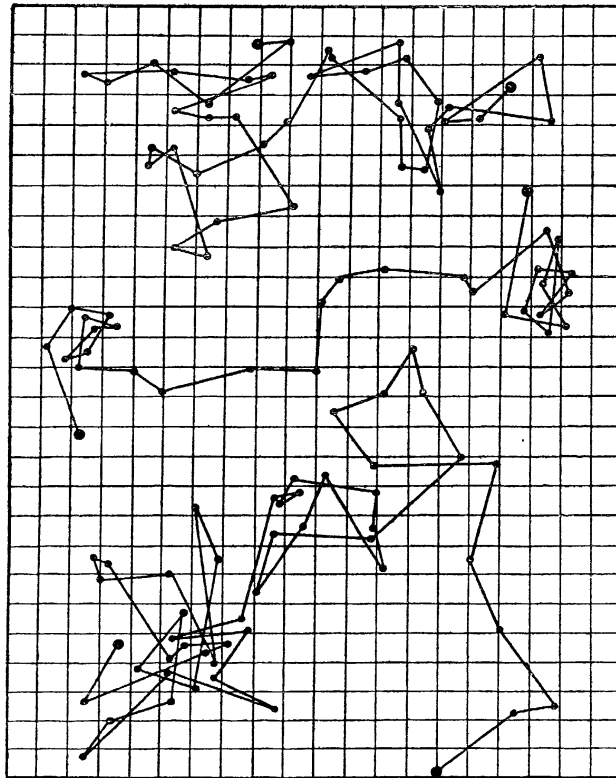
Fig. 5.

11. — Sur la figure ci-jointe on voit, à un gros-sissement tel que 16 divisions du quadrillage repré-

Figure 1.1: Typical Brownian motion trajectories recorded by Jean Perrin in 1909 [9]. The image is taken from the original paper.

---

* The concept of random walk was introduced by Karl Pearson in a query sent to Nature in 1905 [**Pearson1905a**] and Lord Reyleigh provided a solution in the same issue
† This was part of his work which ultimately landed him a Nobel prize in 1926.

This experimental proof of random walk approach to Brownian motion also drew a direct link between the microscopic dynamics of small particles in suspension, through their mean squared displacement, and macroscopic quantities like the diffusion coefficient, or the Avogadro's number; between discrete random walks and continuous diffusion. It has been capable to effectively explain the transport processes which have some element of randomness. Basically to derive the diffusion equation, the starting point of nearly all analysis of transport lies in a random walk model. The true interdisciplinary nature of this formalism can be seen in its vast applications in different scientific disciplines from polymer physics to astrophysics and biology and from mathematics to finance and engineering. As a result, Brownian motion has been extensively studied, particularly in the second half of the last century [10]. However, many questions have emerged since dealing with complex systems within these disciplines, calling for modern treatments.

1.2 Anomalous diffusion

The linear time dependence of the mean squared displacement in equation 1.2 is an immediate consequence of the central limit theorem and stochastic nature of the underlying random processes. This main characteristic of Brownian motion is not valid anymore, when the assumption of central limits theory breaks down. In this case, random walks exhibit a different behaviour where this quantity is not linearly dependent on time. To understand this behaviour, we need to recall that relaxation processes in dynamical systems. Classically, they can be described in term of the exponential function [11]

$$\phi(t) = e^{-\frac{t}{\tau}} \ , \ t \geqslant 0, \tag{1.3}$$

where τ is the time required for the system to reach equilibrium. This equation is often referred to as the Maxwell-Debye relaxation [11–13]. It is derived from the solution of the relaxation equation $\frac{d}{dt}\phi(t) = -\tau^{-1}\phi(t)$ with the normalised initial condition $\phi(0) = 1$. Now let us consider normal diffusion as a standard Markovian model, in which the spreading of random walkers are determined by the diffusion equation with K as the diffusion constant

$$\frac{\partial P}{\partial t} = K\frac{\partial^2}{\partial x^2}P(x,t), \tag{1.4}$$

The solution of this equation would give us the probability density function (PDF) $P(x,t)$ in the form of a normalised Gaussian distribution

$$P(x,t) = \sqrt{4\pi Kt} \cdot \exp(-\frac{-x^2}{4Kt}), \tag{1.5}$$

And by considering the Fourier transform of P ($P^*(k,t)$), a relaxation function can be then defined through

$$\phi(t) = P^*(k,t) = e^{Kk^2t} \ , \ t \geqslant 0, \tag{1.6}$$

complying with Maxwell-Debye pattern. However, this relation is not always applicable when investigating the dynamical properties of disordered complex systems. These systems which were accurately described as "structures with variations" by Goldenfeld and Kadanoff [14], are highly sensitive to the point of view of the observer *i.e.* the scale of observation. They consist of a diverse collection of elementary units which are strongly interconnected. This correlated disorder of the medium affects the nature of diffusion process, making it anomalously faster or slower. It can also induce memory effect to the transport process and therefore, the evolution in time within these systems deviates from the corresponding standard laws, such as Eq. 1.3 [1, 15]. As a result, the diffusion process in complex systems might not obey the Gaussian statistics anymore, implying the breakdown of central limit theorem (CLT). Subsequently, the mean squared displacement (MSD) would no longer be linear in time, giving rise to what is called an

anomalous diffusion. In this study, we will focus on the case where CLT fails due to broad distributions or long range temporal correlations (non-Markoffian processes). This is the most common anomalous behaviour and can be defined by a power-law formulation

$$\langle x^2(t) \rangle \sim K_\alpha t^\alpha, \tag{1.7}$$

where α is a real positive number and K_α is the generalised diffusion coefficient with the dimension $[K_\alpha] = m^2/s^\alpha$ and inherently depends on anomalous diffusion exponent [*] (α). As the mostly non-Gaussian statistics of underlying microscopic processes in complex systems dictates, this type of anomalous diffusion lies on the assumption of the Lévy-Gnedenko-Kolmogorov generalised limit theorem for the sums of independent and identically distributed random variables without the hypothesis of finite variance [16–20]. As a result of this treatment, we can obtain the exponent α, or anomaly parameter, which characterises different domains of anomalous transport as summarised in Figure 1.2.
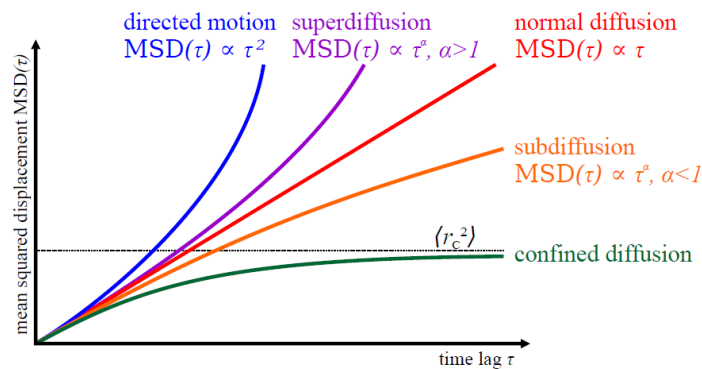
Figure 1.2: Mean squared displacement for different categories of anomalous diffusion.

Different modes of anomalous diffusion

On the macroscopic level enhanced diffusion *i.e.* superdiffusion where $\alpha > 1$ has a more dominant role. In particular, the domain $1 < \alpha < 2$ or the sub-ballistic category has been extensively studied and recognised in different areas *e.g.* spreading of infectious diseases and parasites [21, 22], intracellular transport by protein motors, cell migration on monolayers [23, 24] and internal vacuoles mobility in the cytoplasm of a family of pathogens [25]. It is also commonly observed in the study of bulk-surface exchange in porous media *e.g.* glasses [26], transport in turbulant plasma [27] as well as population's mobility pattern [28]. Two interesting examples of the latter are the famed flight pattern of an albatross [29, 30] and spider monkeys' motion trajectories [31]. In a recent study, it was successfully shown that a superdiffusive process almost at the ballistic limit ($\alpha = 2$) governs the behaviour of the members of the parliament for Brazilian Chambers of Deputies [32]. Ballistic diffusion can be described by the wave equation and active transport [11, 33] and on average it behaves as a Newtonian motion with constant velocity. Processes with an anomaly parameter greater than two ($\alpha > 2$) are also prevalent in chaotic and far from equilibrium systems. Historically it was the first type of anomalous diffusion that has been reported by Richardson in his treaties on pair diffusion in fully developed turbulence in 1926 [1, 34, 35].

Another type of anomalous diffusion which is the main focus of our study is subdiffusion where $\alpha < 1$. Montroll and Scher theoretically examined this domain of anomalous diffusion for the first time, in their study of the dispersive transport in amorphous semiconductors [1, 36]. Their continuous time random walk approach provided an accurate description of observed phenomena in numerous experiments [37–43]. It was the beginning for elaborated investigations of systems exhibiting subdiffusive

---

[*] We refer to it as anomaly parameter in this monograph.

dynamical behaviours. For example, the diffusion of hydrogen in metals [44], charge carrier transport in semiconductor alloys [37, 41–43], the motion of bright spots on the Sun [45], the time-dependent transport of cosmic rays [46–48], the dynamics of a bead in a polymeric network [49, 50], or protein transport in cells and the crowding effect [21, 51–54]. The emergence of subdiffusion is prominently attributed to the crowding-induced viscoelasticity of the environment [21] and therefore it can be used as a tool to extract physical quantity of a complex medium and describe its heterogeneity [55].

1.3 Cell as a model system

Higher spatial and temporal resolution, brought on by the technical advancement of experimental setups, significantly facilitated the exploration of structural and dynamical properties of complex systems. As a result, random motions, which have been more widely observed in these systems, became a subject of increased interest. In particular, the recent progress in light microscopy and labelling techniques have given rise to numerous studies of different regimes of diffusion and transport mechanisms (Figure 1.3) in biological systems and cellular interior.
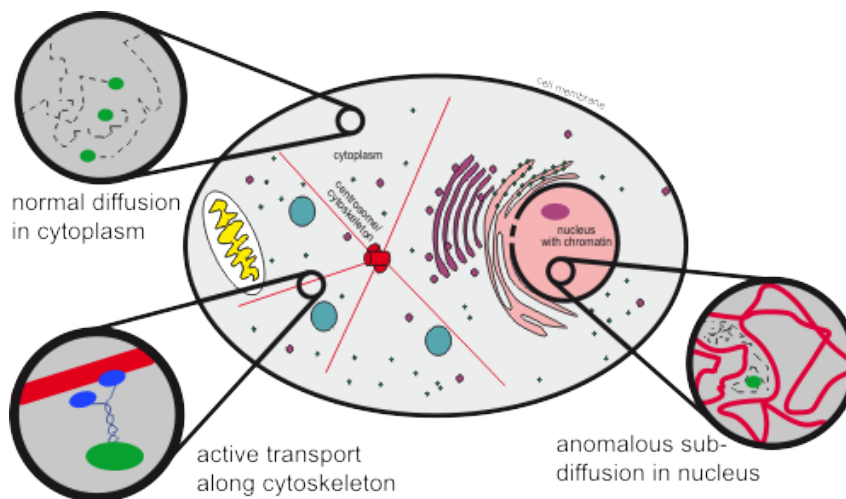
Figure 1.3: Schematic of different types of diffusion in a cell

Despite being the subject of extensive research in life sciences, very little is known about many basic aspects of cell as the main constituent of living organisms. For this reason, it is one of the most suitable platforms for physicists to study a variety of phenomena prevalent in complex systems.

The interior of eukaryotic cells *, such as mammalian cells, which are typically between 10 µm and 100 µm [56], is filled with a concentrated aqueous solution called cytoplasm. Proteins, sugar molecules, lipids, salt ions and other solvents are dissolved in this seemingly unstructured liquid. However, upon closer examination, it becomes clear that cytoplasm is indeed structured in many length scales. From organelles like the mitochondria, endosomes and Golgi apparatus in µm scale to 100 nm scale of endoplasmic reticulum (ER), microtubuli and actin filaments [53]. This collection of cellular compartments with their specific functionalities, together with cytoskeleton, produce a dense viscoelastic network through which interacting biomolecules must navigate [57, 58]. This crowded environment was revealed by electron microscopy studies of cells (illustrated in Figure 1.4). [58, 59]

Cells are dynamically reorganising themselves during their normal functions such as division, adhesion and motility, thanks to their adaptive cytoskeleton network. At the same time, all of these functions affect intracellular compartments and, more specifically, cause structural reorganisation within the

---

* There are two categories of cell types: prokaryotic (bacteria and archaea) and eukaryotic. eukaryotes have a nucleus enclosed within a membranes unlike prokaryotes which have no membrane-bound organelles
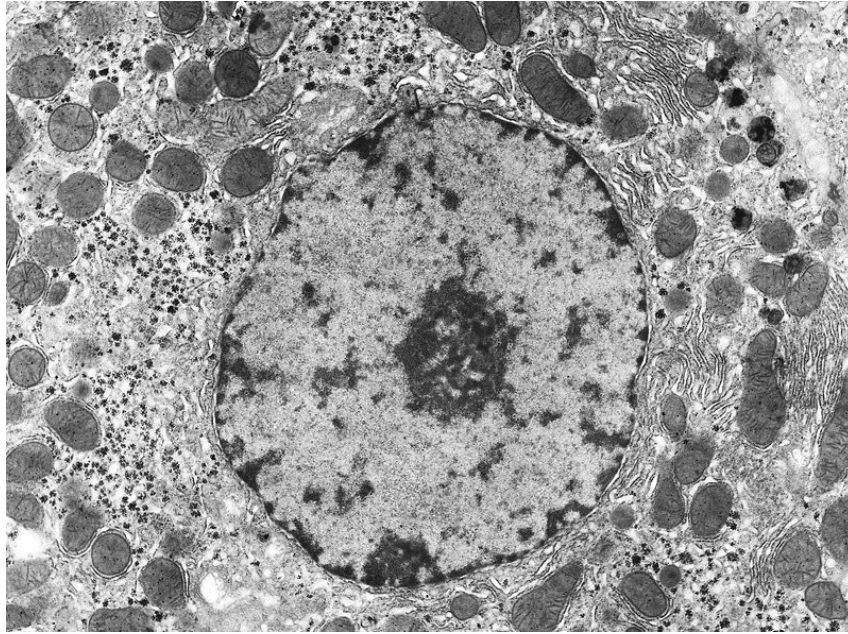
Figure 1.4: A resolved electron microscopy image of a eukaryotic cell showcasing the shape of different organelles

nucleus, which contains genomic material and is the largest organelle of a eukaryotic cell [57]. Still, the mere existence of an architecture similar to the cytoskeleton in the nucleus was disputed for half a century [60]. The first hint at finding a resolution was the discovery of nuclear intermediate filament (IF) proteins, named lamins, in 1978 [61]. Later, biochemical studies of the nucleus showed its complex mechanical properties and this, added to the evidence of mechanical coupling of intranuclear structures and cytoskeleton, strongly suggested the existence of a complex viscoelastic network, rivalling that of the cytoskeleton, albeit stiffer *[62, 64]. This nuclear matrix, or nucleoskeleton, forms a crowded environment that is highly organised and complex and one which actively influences the movement of macromolecules. These characteristics, and the fact that the functional role of most nuclear structures remains unidentified [57], renders nucleoplasm an interesting model study, not only in cell biology, but also in condensed and soft matter physics.

Intranuclear dynamics

Each single nucleus of a eukaryote contains its whole genetic information, its genome, in one or several DNA (deoxyribonucleic acid) molecules. DNA is a long, double-stranded polymer which is compacted in the very limited volume of the nucleus. Therefore, it has to be tightly packaged and forms a higher order structure called chromatin. To understand the magnitude of the discrepancy between the length of DNA and the size of the nucleus, consider a human DNA which is around 2 m fits into a nucleus having a typical radius of few microns, and it is occupying only 10% of it. Expression of each gene of this massive genetic material is controlled by transcription and repression factors as well as the accessibility of the gene for the necessary molecules. The chromatin spatial organisation within the nucleus further regulates the gene expression [65]. Moreover, the dynamic movements of chromatin and its interaction with other macromolecules that are abundant inside the nucleus, play a crucial role in gene regulation [66, 67]. However, the mechanism of this mobility and interaction is not very well understood. In fact, it was only over the past 10 years that the conventional view of chromatin as a static regular structure has shifted to a dynamic and highly variable configuration [68]. The dynamics that are driven both by binding

---

* The measured stiffness of nucleoskeleton for animal cells is roughly fivefold to tenfold higher than that of the cytoskeleton, making it the dominant skeletal element in mammalian cells [60, 62, 63]

of protein complexes as well as the physical effects including macromolecular crowding and depletion attraction [65, 69].

Nuclear structures appear to be self-organising, and unlike cytoplasmic organelles, they are not bounded by a membrane [66, 67]. In the interphase nuclei for example, chromatin is arranged in the nucleus with loose spatial specificity. It is segregated into distinct gene-rich, less densely packed regions called euchromatin and inactive and transcriptionally repressed, compact regions referred to as heterochromatin [70, 71]. Proteinaceous nuclear bodies are scattered amongst these chromatin domains. Their functionalities are the subject of active research but recently it was shown that substantial fraction of the genome displays preferential organisation with respect to these nuclear bodies [72]. Nuclear bodies can act as hubs that shape the overall packaging of DNA in the nucleus. Other cellular factors that read, copy and maintain the genome are also organised in a rather sophisticated manner. Transcription factors, structural chromatin proteins and RNA processing factors are localised in specific nuclear domains. In addition to the heterogeneous distributions of chromatin condensation and protein concentrations, the interconnection with the nuclear matrix (nucleoskeleton) builds an intricate and dynamic network within the nucleus through which macromolecules such as proteins, transcriptional activators, polymerases, repressors and also RNA molecules must find their targets [70]. Understanding the nature of intranuclear dynamics is indispensable for understanding nuclear functions like gene expression, DNA replication, recombination and repair and RNA splicing [73].

A-type lamins
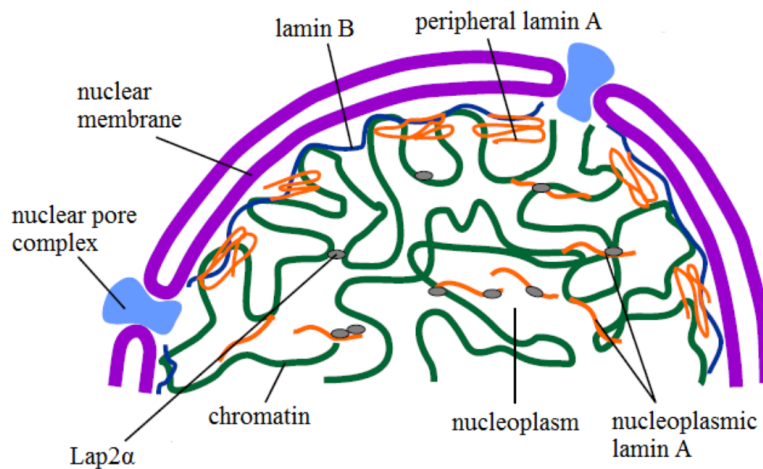
Figure 1.5: A-type lamins in the cell nucleus. A schematic drawing of the cell nucleus. Beside the lamin structure in the lamina at the nuclear envelope, smaller molecules of A-type lamin can be recognised in the nucleoplasm.

The major components of nucleoskeleton are lamin filament networks. They are the most studied and characterised element of nucleoskeleton. This is due to the fact that over twenty human diseases [*], including dilated cardiomyopathy with variable muscular dystrophy, Dunnigan-type familial partial lipodystrophy (FPLD2), Hutchinson-Gilford progeria syndrome (accelerated ageing disease) and Emery Dreifuss muscular dystrophy are linked to the mutations in the LMNA gene, which is the one encoding A-type lamins [60, 74, 75]. Mammals express A-type (lamin A and C) and B-type lamins (lamin B1 and B2). The lamins first characterised biochemically as prominent 60 to 80 kDa proteins and ultimately identified as intermediate filament (IF) proteins by sequence homology [61, 76–81]. Intermediate filaments are assembled fibres with an average diameter between 6 to 12 nm. On the molecular level, A-type lamins

---

[*] Laminopathies

generally resemble B-type lamins over the amino-terminal head and central rod domain but have an expanded carboxy-terminal tail domain containing 90 unique amino acids [76]. Lamin proteins are the major components of the peripheral nuclear lamina. They form a dense meshwork of filaments near the inner nuclear membrane, which interacts with a large number of binding partners. They ultimately form the nuclear lamina together with these binding partners . In addition to maintaining the structural integrity of nucleus, it has been shown that lamins are involved in several other cellular functions including chromatin reorganisation, DNA repair and nuclear assembly among others [82, 83].

Although A-type and B-type lamins can interact in vitro [84], they form separate, functionally distinct filament networks. Other than the lamina network where the lamins are mostly concentrated, they are also distributed throughout the nucleoplasm (Figure. 1.5). A-type lamins, in particular, were shown to exist in different states within nuclear compartments. The assembly state of nucleoplasmic lamins remains elusive as different studies found them either in a rather unstructured veil of proteins or short fibrous structures [85–91]. It has also been shown that nucleoplasmic lamin complexes are considerably more mobile than peripheral lamins [89–91]. Current data shows that most of the A-type lamins in the nuclear interior exist in a mobile low-assembly state and differs significantly from their structure at the nuclear periphery [92]. There has been many speculations around the functions of nucleoplasmic lamins. From nuclear house keeping functions to scaffolding the chromatin and affecting the transcription. Nevertheless, the exact functions of nucleoplasmic A-type lamins are still unknown.

1.4 Motivation and outline of the thesis

In order to understand a complex system, we are required to extract meaningful physical quantities. For that we need to focus on the right level of parametrisation of the system and refine our questions. In this monograph we analysed the dynamics of chromatin in the viscoelastic environment of nuclear interior and examined its co-mobility and interconnection with nucleoplasmic lamin A. For this reason, we employed all three modes of investigations (experimental, computational and theoretical) [14] to answer two fundamental questions regarding nucleoplasmic A-type lamins:

1. Do nucleoplasmic A-type lamins interact with chromatin in live mammalian cells?
2. How do these proteins affect the viscoelasticity of intracellular environment and the nature of diffusion of macromolecules ?

Characterising the diffusion of particles requires following their motion. This can be done on labelled molecules in an optical microscope by exciting their fluorescence and detecting the emitted photons. Then, the motion of single molecules can be followed by two principal approaches: tracking of individual particles and analysis of their trajectories, or the statistical analysis of the fluctuations of fluorescence intensity at fixed positions in the sample. The latter approach is known as fluorescence correlation spectroscopy (FCS). Using light sheet illumination with a fast two-dimensional detector then allows one to do these statistical analyses on each single image pixel of an entire plane simultaneously. This technique can be extended to fluorescence cross-correlation spectroscopy (FCCS) to identify the comobility between two molecules tagged by different fluorophores as well as spatial cross-correlation spectroscopy to pinpoint the spatial arrangement and conformation of the tagged particle. The principle of fluorescence (cross-)correlation spectroscopy will be introduced in Chapter 2 and in Chapter 3 the results of our measurements in different systems will be presented.

Chapter 4 is dedicated to a simulation framework to describe the observed effect. In this simulation, chromatin is modelled as a chain polymer undergoing Brownian dynamics. The chain dynamics is described by the Langevin equation taking into account the effect of interconnection with A-type lamins on the mobility of the chain.

Finally we conclude the thesis in Chapter 5 by discussing the results and offering a possible outlook for further studies. Parts of this thesis is already published in [54].

2 Principles of fluorescence (cross-)correlation spectroscopy (F(C)CS)

Initially invented by Magde et al. to measure chemical reaction rates and binding of ehidium bromide onto DNA [93], fluorescence correlation spectroscopy (FCS) has been developed to study the kinetics processes through statistical analysis of fluctuations in equilibrium. To detect the fluctuation, a fluorescence signal is coupled to different states of the system so any spontaneous fluctuation would result in a change in fluorescence. These random fluctuations can be translated into an autocorrelation function, which carries information on the characteristic time scales and relative weight of different transition in the system [94]. With an appropriate model of the system dynamics, different kinetic rates can be quantified. In our particular example, the random motion of fluorescently tagged particles causes fluctuations in fluorescence signal and processing these fluctuations can unravel the diffusion dynamics in the sampling volume. Figure 2.1 summarises the main principle behind this technique.
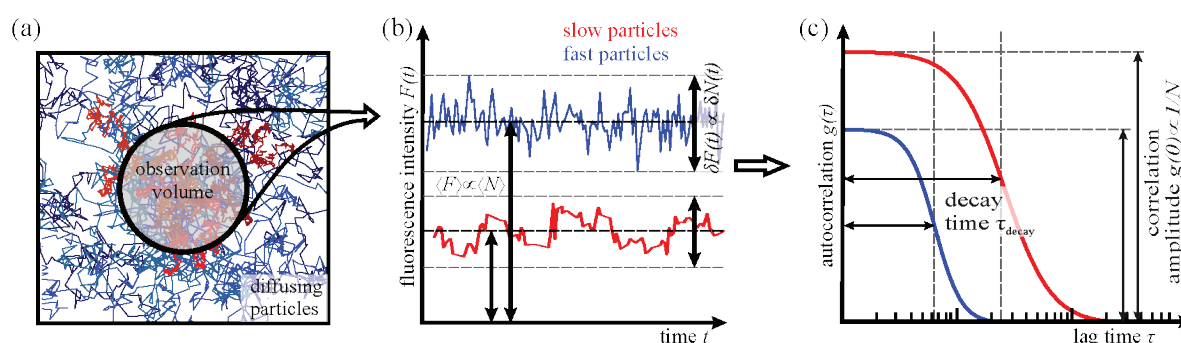
Figure 2.1: Illustration of the statistical analysis of fluctuations in FCS. (a) The sampling volume with tagged particles diffusing at different rates. (b) The fluorescence intensity traces as measured from the sample at (a), showing the fluctuation δF around the mean intensity $\langle F \rangle$. (c) Autocorrelation functions $g(\tau)$ for both tagged particles where the decay times τ_{decay} are defined as $\tau = g(0)/2$. The figure is taken from [95]

Although the principal ideas behind FCS and its application were well established in the 70s, the technique was not sensitive enough to detect the fluorescence effectively, requiring high concentration of fluorescent molecules [94]. It was with the introduction of the confocal illumination scheme in FCS in 1993 by Rigler et al. [96] boosting the detection sensitivity to a single molecule level, that it started to gain back the attention of the scientific community. This renewed interest resulted in many publications and short reviews of the applications of FCS in different fields of physics and biology in the years after [94, 97–99]. Coupling FCS with light sheet fluorescence microscopy brought a larger field of view and simultaneous detection of the signal at spatially apart positions of the sample [95, 100–104]. This is the method of choice to analyse the dynamics of diffusing particles in the viscoelastic media in this thesis.

Combining FCS with other super resolution nanoscopy techniques has already attracted interests in recent years, promising an even better characterisation of the dynamics of small molecules in foreseeable future.

2.1 Basic definitions

Autocorrelation function

Let us assume our sample contains only a few fluorescent particles at any time ($N(t)$). The detected fluorescence intensity in the observation volume ($F(t)$) is then proportional to this particle number. Due to the diffusion of the particle and presumption of normal Brownian motion, $N(t)$ is fluctuating ($\delta N(t)$) around its mean $\langle N \rangle$.

$$N(t) = \langle N \rangle + \delta N(t) \quad \Rightarrow \quad F(t) = \langle F \rangle + \delta F(t) \tag{2.1}$$

$$\langle \delta N(t) \rangle = \langle \delta F(t) \rangle = 0,$$

Accordingly, we define the autocorrelation function as follows

$$g(\tau) = \frac{\langle \delta F(t) \cdot \delta F(t + \tau) \rangle}{\langle F(t) \rangle^2} = \frac{\langle F(t) \cdot F(t + \tau) \rangle}{\langle F(t) \rangle^2} - 1 \quad , \quad \tau > 0, \tag{2.2}$$

where τ is the time lag and the averaging operation $\langle \cdot \rangle$ is a time average

$$\langle x(t) \rangle = \lim_{T \to \infty} \frac{1}{T} \int_0^T x(t)dt, \tag{2.3}$$

An interesting characteristic of $g(\tau)$ is that it will be equal to zero in case of random white noise because then the correlation function would be proportional to the noise fluctuation and is 0 for all different time lags $\tau > 0$. As is clear from its definition, $g(\tau)$ measures the similarity of the signal $x(t)$ to itself (hence the term "auto" in autocorrelation) by a shift in time $x(t + \tau)$. In the case of random Brownian motion of particles, this function is non-zero over a given time (τ_D). It is the characteristic time that the particles stay in the observation volume, called the dwell time. In the case of normal diffusion, this time is inversely dependent on the diffusion coefficient of the particles (Eq. 1.2).

$$\tau_D \propto \frac{\sqrt[3]{V_{obs}^2}}{D}, \tag{2.4}$$

During the dwell time, the self-similarity in the fluctuations appears as a decay of autocorrelation function from $g(0) > 0$ to $g(\infty) = 0$. The half-life of this decay can also be approximated from Eq. 2.3.
Knowing the Poissonian nature of fluctuations, a relation can be drawn between the autocorrelation function at $\tau = 0$ and the averaged number of observed particle.

$$g(0) = \frac{\langle \delta F^2(t) \rangle}{\langle F(t) \rangle^2} \propto \frac{\langle \delta N^2(t) \rangle}{\langle N(t) \rangle^2} = \frac{1}{\langle N(t) \rangle}, \tag{2.5}$$

since the mean and the variance of a Poissonian event are the same ($\langle \delta N^2(t) \rangle = \langle N(t) \rangle$).

Point spread function

One of the limitations of any optical setup is the diffraction of light at the apertures of its objectives. Therefore, a point in the object plane is seen as a blurred circle or an airy disc in the detection plane. The three dimensional shape of this airy disc is defined by the point spread function (PSF_{fl}). Therefore the

intensity distribution of the signal detected in the optical system is described by a convolution of the distribution of fluorophores in the object plane ($c(\vec{r}, t)$ with the $\text{PSF}_{\text{fl}}(\vec{r})$ of the optical setup

$$I(\vec{r}, t) = c(\vec{r}, t) \circledast \text{PSF}_{\text{fl}}(\vec{r}), \tag{2.6}$$

It is possible to analytically approximate the point spread function using the Debye diffraction theory [105]. For this reason the numerical aperture (NA) of the system should be considered, which is directly related to the focal length (f_{obj}) and the aperture diameter (d_{obj}) of the lens or objective and the diffraction index of the medium (n).

$$\text{NA} := n \cdot \frac{d_{\text{obj}}}{f_{\text{obj}}} = n \cdot \sin(\alpha) \quad \Rightarrow \quad \text{NA} \leqslant n, \tag{2.7}$$

Here 2α is the opening angle of the objective. The numerical aperture is an indicator of the focusing power of the lens. We can now introduce new coordinate based on the NA of the system,

$$u \equiv u(z) = \frac{2\pi\text{NA}^2}{n\lambda} \cdot z \quad \text{and} \quad v \equiv v(x, y) = \frac{2\pi\text{NA}}{\lambda} \cdot \sqrt{x^2 + y^2}, \tag{2.8}$$

where λ is the wavelength of fluorescent signal. (PSF_{fl}) then can be numerically approximated as modulus squared of electrical field distribution around the focus h(u,v).

$$\text{PSF}_{\text{fl}}(u, v) = |h(u, v)|^2 \tag{2.9}$$

In the z-plane and xy-plane, (PSF_{fl}) would get a simplified analytical forms [95, 105].

$$\text{PSF}_{\text{fl}}(u, 0) \propto \left(\frac{4\sin(\frac{u}{4})}{u}\right)^2 \quad , \quad \text{PSF}_{\text{fl}}(0, v) \propto \left(\frac{2J_1(v)}{v}\right)^2, \tag{2.10}$$

where $J_1(\cdot)$ is a Bessel function of the first kind. From Eq. 2.10, it is possible to calculate the size of the focus as the $1/e^2$ half widths w_{xy} and w_z of the central maximum

$$w_{xy} \approx 0.82 \cdot \frac{\lambda}{\text{NA}} \quad , \qquad w_z \approx 2.80 \cdot \frac{n\lambda}{\text{NA}^2} \quad , \tag{2.11}$$

This definition of (PSF_{fl}) is the standard definition that is usually used in literature on fluorescence correlation spectroscopy. We use this definition to characterise the point spread function of the light sheet microscope system in the next section.

2.2 Modeling fluorescent light in a microscope

We will now consider a simplified fluorescen microscope model presented in Figure 2.2 to establish the theoretical framework of FCS. Let assume that there are N_χ number of species χ in the sampling volume V_{obs}. We define $\vec{r}_i$ as the trajectory vector of ith particle for $i = 1 \ldots N_\chi$. These trajectories are not known per se but their statistical characters, assuming they are undergoing random motions, can be well recognised with functions like mean squared displacement function (MSD). The relation for the local concentration distribution of χ can be written as

$$c_\chi(\vec{r}, t) = \frac{1}{V_{\text{obs}}} \cdot \sum_{i=1}^{N_\chi} \delta\left(\vec{r} - \vec{r}(t)\right), \tag{2.12}$$

The particles are illuminated with an intensity distribution I_γ where γ denotes the detection channel and the resulting signals from their excited state are detected in a detection objective by a probability defined with a detection efficiency distribution $\Omega_\gamma(\vec{r})$. These two distributions are not observable independently and therefore they are usually combined into a single function called "Molecular Detection Efficiency" function (MDE)

$$\text{MDE}(\vec{r}) := I_\gamma(\vec{r}) \cdot \Omega_\gamma(\vec{r}), \tag{2.13}$$

This function is proportional to the rate of the photons expected from a fluorophore at position $\vec{r}$. For a given optical setup, it is calculated from its PSFs. The geometry of the detectors (*e.g.* square pixels of a camera) also plays a role in its determination. For confocal setups, 3-dimensional symmetric Gaussian function with width w_γ and height z_γ gives a reliable approximation of PSF_{fluo}. Hence, MDE

$$\text{MDE}_{\text{confocal},\gamma}(\vec{r}) = I_0 \cdot \exp\left(2 \cdot \frac{x^2 + y^2}{w_\gamma^2} - 2 \cdot \frac{z^2}{z_\gamma^2}\right), \tag{2.14}$$
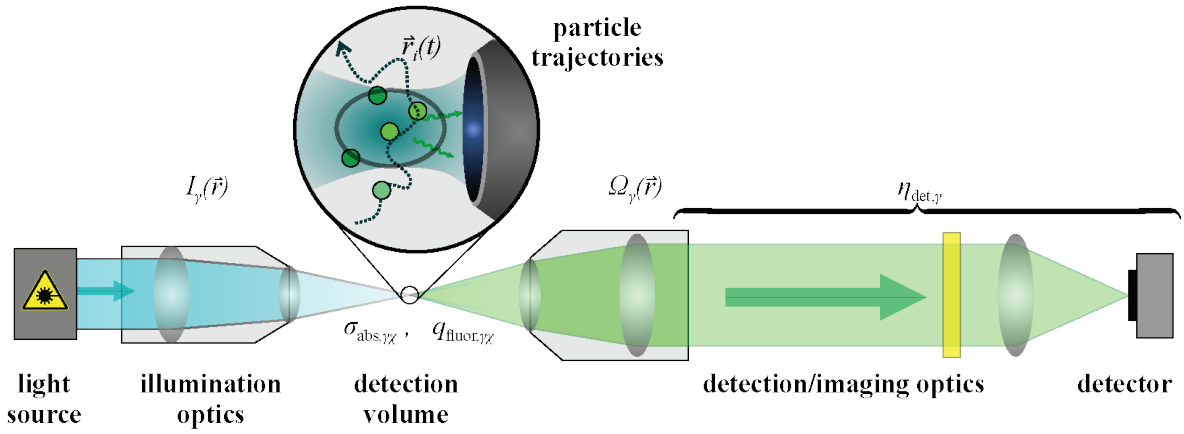
Figure 2.2: Schematic presentation of a simplified optics model for FCS theory. The illumination objective focuses the light into an intensity distribution I_γ. The resulting signals are detected on a detection optic characterised by its detection efficiency $\eta_{\text{det},\gamma}$ and its detection efficiency distribution $\Omega_\gamma(\vec{r})$. In the sampling volumes particles of species χ are moving randomly in a trajectory denoted by $\vec{r}$ and each have an absorption cross section $\sigma_{\text{fluo},\gamma,\chi}$ and a fluorescence quantum efficiency $q_{\text{fluo},\gamma,\chi}$. The figure is taken from [95]

In a properly aligned single plane illumination microscopy (SPIM) setup the side lobes of the light sheet are minimised by spatial filtering of the laser beam to resemble a Gaussian shape of an intensity profile in the z-direction comparable to the confocal case [101, 103]. Assuming a good alignment and taking into account the pixel width a of the camera, the final form of MDE for SPIM will be

$$\text{MDE}_{\text{SPIM},\gamma}(\vec{r}) = I_0 \cdot (h_{\text{pixel}} \circledast \text{PSF}_{\text{SPIM},\gamma})(\vec{r}) = \int\!\!\!\int\limits_{-a/2}^{a/2} \text{PSF}_{\text{SPIM},\gamma}(\vec{r} - \vec{r}')dxdy, \tag{2.15}$$

where $h_{\text{pixel}}(\vec{r})$ is the characteristic function, describing the camera pixel.

$$h_{\text{pixel}}(\vec{r}) = \delta(z) \cdot \begin{cases} 1 & -\frac{a}{2} \leqslant x, y \leqslant \frac{a}{2} \\ 0 & \text{otherwise} \end{cases} \tag{2.16}$$

The integral in Eq. 2.15 can be solved analytically, therefore

$$\text{MDE}_{\text{SPIM},\gamma}(\vec{r}) = I_0 \cdot \frac{\left(\text{erf}\left(\frac{a-2x}{\sqrt{2}\cdot w_\gamma}\right) + \text{erf}\left(\frac{a+2x}{\sqrt{2}\cdot w_\gamma}\right)\right) \cdot \left(\text{erf}\left(\frac{a-2y}{\sqrt{2}\cdot w_\gamma}\right) + \text{erf}\left(\frac{a+2y}{\sqrt{2}\cdot w_\gamma}\right)\right)}{\left(\text{erf}\left(\frac{a}{\sqrt{2}\cdot w_\gamma}\right)\right)^2} \cdot \exp\left(-2 \cdot \frac{z^2}{z_\gamma^2}\right), \tag{2.17}$$

where erf(·) is the error function, defined as

$$\text{erf}(x) = \frac{2}{\sqrt{\pi}} \int_0^x \exp(-t^2)dt \tag{2.18}$$

Note that $\text{MDE}_{\text{SPIM},\gamma}$ given in Eq. 2.17, deviates significantly from Gaussian form if the pixel width of the camera is much larger than the lateral width w_γ of PSF. This is shown in Figure 2.3
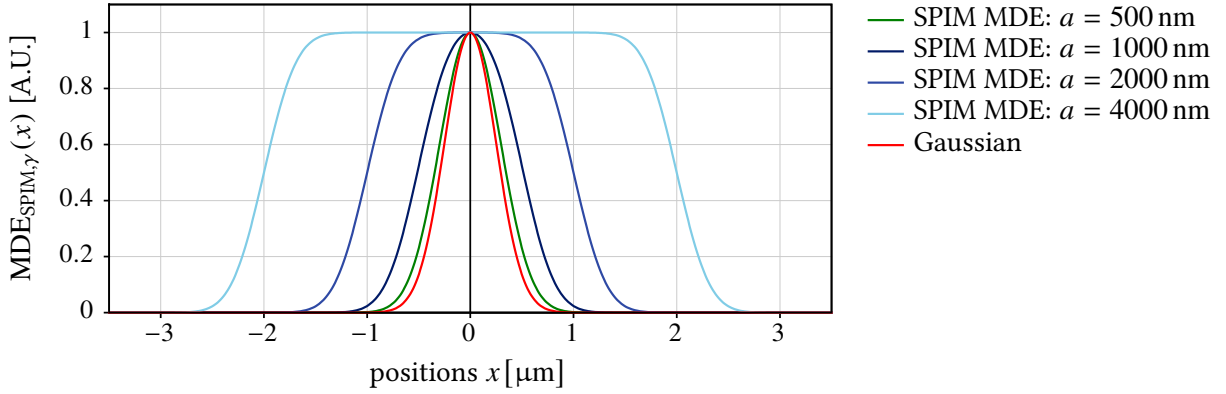
Figure 2.3: MDE of SPIM along one coordinate axis for different pixel width. The width of PSF for all the plots is the same $w_\gamma = 500\,\text{nm}$. The figure is taken from [95]

Now we are equipped to calculate the autocorrelation function. The first step would be examining the fluorescence intensity time trace $F_\gamma(t)$ expected from a fluorophore concentration($c_\chi(\vec{r}, t)$). We need to assign an absorption cross section $\sigma_{\text{det},\gamma}$ and a fluorescence quantum yield $q_{\text{fluo},\gamma,\chi}$ to each species for quantifying the fluorescence emitted by a single fluorophore. Then, taking into account the detection efficiency of our optical setup $\eta_{\text{det},\gamma}$, which is the representative for any signal loss due to the filters used in the detection beam path or in general in optical surface, we are able to define a single detection efficiency $\eta_{\chi,\gamma}$ for each particle χ in species space $\mathbb{S}$ in channel γ as

$$\eta_{\chi,\gamma} \equiv \eta_{\text{det},\gamma} \cdot \sigma_{\text{det},\gamma} \cdot q_{\text{fluo},\gamma,\chi}. \tag{2.19}$$

Then $F_\gamma(t)$ will be

$$F_\gamma(t) = \iiint_{-\infty}^{\infty} \text{MDE}_\gamma(\vec{r}) \cdot \sum_{\chi \in \mathbb{S}} \eta_{\chi,\gamma} \cdot c_\chi(\vec{r}, t)\ dV. \tag{2.20}$$

Since concentration is proportional to the detected fluorescent intensity, it can be defined as a fluctuation of concentration around the average concentration of fluorophores in an analogous term with Eq. 2.1

$$c_\chi(\vec{r}, t) = \langle c_\chi \rangle + \delta c_\chi(\vec{r}, t) \tag{2.21}$$

Because of the linearity of Eq. 2.20, we can find a relation for $\delta F_\gamma(t)$.

$$\delta F_\gamma(t) = \iiint\limits_{-\infty}^{\infty} \mathrm{MDE}_\gamma(\vec{r}) \cdot \sum_{\chi \in \mathbb{S}} \eta_{\chi,\gamma} \cdot \delta c_\chi(\vec{r},t) \; dV. \tag{2.22}$$

The FCS autocorrelation function in Eq. 2.2 can be rewritten for a color channel γ, taking into account Eq. 2.20 and Eq. 2.22 as

$$g_\gamma(\tau) = \frac{\sum\limits_{\chi \in \mathbb{S}} \eta_{\chi,\gamma}^2 \iiint\limits_{-\infty}^{\infty} \mathrm{MDE}_\gamma(\vec{r}) \cdot \iiint\limits_{-\infty}^{\infty} \mathrm{MDE}_\gamma(\vec{r}') \cdot \langle \delta c_\chi(\vec{r},t) \cdot \delta c_\chi(\vec{r},t) \rangle \; dV \; dV'}{\left(\sum\limits_{\chi \in \mathbb{S}} \eta_{\chi,\gamma}^2 \iiint\limits_{-\infty}^{\infty} \mathrm{MDE}_\gamma(\vec{r}) \cdot \langle c_\chi(\vec{r},t) \rangle \; dV \right)^2} \qquad \square \tag{2.23}$$

This relation is derived from the linearity of integral, from which the linearity of averaging is also deduced. Another important assumption for this relation to be true is the statistical independence of the concentration fluctuations for two different species *i.e.* $\langle \delta c_\chi(\vec{r},t) \cdot \delta c_{\chi'}(\vec{r},t) \rangle = 0$.

Another quantity that would be helpful to determine the dynamics of the particle is the volume which is efficiently observed. This volume is called the effective volume $V_{\mathrm{eff},\gamma}$ and can be defined with respect to the number of fluorophores and their concentration in the focus

$$V_{\mathrm{eff},\gamma} := \frac{\langle N_\chi \rangle}{\langle c_\chi \rangle}. \tag{2.24}$$

This is an important optical characteristic that can be used to calculate the dwell time of our tagged particle. To find a relation, we will again use Poisson distribution characteristic, but this time for the concentration of the particles in the focus.

$$\langle \delta c_\chi(\vec{r},t) \cdot \delta c_\chi(\vec{r},t) \rangle = \langle \delta c_\chi^2(\vec{r},t) \rangle \cdot \delta(\vec{r} - \vec{r}') = \langle c_\chi(\vec{r},t) \rangle \cdot \delta(\vec{r} - \vec{r}') \tag{2.25}$$

Now, considering the amplitude of autocorrelation function at $\tau = 0$ and assuming that the concentration does not change significantly over the observation volume, an explicit relation can be derived based on Eq. 2.5.

$$g_\gamma(0) = \frac{1}{\langle N_\chi \rangle} = \frac{\sum\limits_{\chi \in \mathbb{S}} \eta_{\chi,\gamma}^2 \cdot \langle c_\chi \rangle \cdot \iiint\limits_{-\infty}^{\infty} \mathrm{MDE}_\gamma^2(\vec{r}) \; dV}{\left(\sum\limits_{\chi \in \mathbb{S}} \eta_{\chi,\gamma}^2 \cdot \langle c_\chi \rangle \cdot \iiint\limits_{-\infty}^{\infty} \mathrm{MDE}_\gamma^2(\vec{r}) \; dV \right)^2}$$

$$= \frac{\sum\limits_{\chi \in \mathbb{S}} \eta_{\chi,\gamma}^2 \cdot \langle c_\chi \rangle}{\left(\sum\limits_{\chi \in \mathbb{S}} \eta_{\chi,\gamma}^2 \cdot \langle c_\chi \rangle \right)^2} \cdot \frac{\iiint\limits_{-\infty}^{\infty} \mathrm{MDE}_\gamma^2(\vec{r}) \; dV}{\left(\iiint\limits_{-\infty}^{\infty} \mathrm{MDE}_\gamma^2(\vec{r}) \; dV \right)^2} = \frac{1}{\langle c_\chi \rangle} \cdot \frac{\iiint\limits_{-\infty}^{\infty} \mathrm{MDE}_\gamma^2(\vec{r}) \; dV}{\left(\iiint\limits_{-\infty}^{\infty} \mathrm{MDE}_\gamma^2(\vec{r}) \; dV \right)^2} \tag{2.26}$$

Combining Eq. 2.24 and Eq. 2.26 we will finally arrive at a formulation for V_{eff}

$$V_{\mathrm{eff},\gamma} = \frac{\left(\iiint\limits_{-\infty}^{\infty} \mathrm{MDE}_\gamma^2(\vec{r}) \; dV \right)^2}{\iiint\limits_{-\infty}^{\infty} \mathrm{MDE}_\gamma^2(\vec{r}) \; dV} \tag{2.27}$$

It is possible to analytically approximate the effective volume for a light sheet from Eq. 2.17

$$V_{\text{eff},\gamma} = \frac{\sqrt{\pi} \cdot a^2 \cdot z_\gamma}{\left(\text{erf}\left(\frac{a}{w_\gamma} \right) + \frac{w_\gamma}{\sqrt{\pi} \cdot a} \left(\exp\left(-\frac{a^2}{w_\gamma^2} \right) - 1 \right) \right)^2}$$ (2.28)

In order to find a relation for the dwell time $\tau_{D,\chi}$ the effective lateral focal area need to be defined [102]. It can be considered as a projection of effective volume in xy-plane

$$A_{\text{eff},\gamma} = \frac{\left(\iint\limits_{-\infty}^{\infty} \text{MDE}_\gamma(x, y, 0) \; dxdy \right)^2}{\iint\limits_{-\infty}^{\infty} \text{MDE}_\gamma^2(x, y, 0) \; dxdy} = \frac{a^2}{\left(\text{erf}\left(\frac{a}{w_\gamma} \right) + \frac{w_\gamma}{\sqrt{\pi} \cdot a} \left(\exp\left(-\frac{a^2}{w_\gamma^2} \right) - 1 \right) \right)^2}$$ (2.29)

Thus, the dwell time of the fluorescence particle in a SPIM setup taking into account Eq. 2.4 can be introduced as

$$\tau_{D,\chi} = \frac{A_{\text{eff},\gamma}}{4D_\chi}.$$ (2.30)

2.3 FCS theory for different types of diffusion

The autocorrelation function can be rewritten on the basis of the diffusion nature of tracers. This will give us an appropriate tool to analyse the experimental data and explore different theory for the observed motions. As it is shown in Eq. 2.23, the particle dynamics can be described by concentration correlation factor $\phi_\chi(\vec{r}, \vec{r}', \tau)$

$$\phi_\chi(\vec{r}, \vec{r}', \tau) \equiv \phi_\chi(\vec{r} - \vec{r}', \tau) := \langle \delta c_\chi(\vec{r}, t) \cdot \delta c_\chi(\vec{r}', t + \tau) \rangle$$ (2.31)

It quantifies the correlation between the concentrations at two different position within the lag time The equivalence in the relation($\phi_\chi(\vec{r}, \vec{r}', \tau) \equiv \phi_\chi(\vec{r} - \vec{r}', \tau)$) is on the assumption that the whole system is shift-invariant and the correlation is only dependent on the positions difference $\vec{r} - \vec{r}'$. If the system is also isotropic, this self correlation function only depends on the length $\|\vec{r} - \vec{r}'\|$. These assumptions are acceptable on the small scales of FCS measurements.

The concentration correlation factor can also be defined with respect to the probability of finding a particle at position r' at time τ if it was initially at position r. This probability distribution is called van-Hove self correlation function ($P_\chi(r, r', t)$) [106]. In an isotropic, invariant system a special case of this function in the form $P_\chi(\cdot, \cdot)$ can be calculated as a Green's function. For the diffusion equation governing the dynamics of $c_\chi(\vec{r}, t)$ (Eq. 1.4, the Green's function is the solution of the PDE for the initial condition $c_\chi(r, 0) = \delta(\vec{r})$ [107]. It then can be used to calculate the general solution $c_\chi(\vec{r}, t)$ for an arbitrary initial condition.

$$c_\chi(\vec{r}, \tau) = c_\chi(\vec{r}, t) \circledast P_\chi(\vec{r}, \tau) = \int \cdots \int c_\chi(\vec{r}, t) \cdot P_\chi(\vec{r}, \vec{r}', \tau) \; \mathrm{d}^d r'$$ (2.32)

where $\circledast$ is a convolution operator and d is the dimension of the system as in Eq. 1.2. The relation for concentration correlation function can be rewritten in terms of P_χ

$$\phi_\chi(\vec{r} - \vec{r}', \tau) := \langle \delta c_\chi(\vec{r}, t) \cdot \delta c_\chi(\vec{r}', t + \tau) \rangle = \langle c_\chi \rangle \cdot P_\chi(r, r', t)$$ (2.33)

In order to incorporate $\phi_\chi(\vec{r} - \vec{r}', \tau)$ in the autocorrelation function, first rewrite its definition

$$g_\gamma(\tau) = \frac{\sum\limits_{\chi \in \mathbb{S}} \eta^2_{\chi,\gamma} G^\chi_\gamma(\tau)}{\left(\sum\limits_{\chi \in \mathbb{S}} \eta^2_{\chi,\gamma} \langle c_\chi \rangle \right)^2}, \tag{2.34}$$

where G^χ_γ is a general, non-normalised correlation function that is defined as follows

$$G^\chi_\gamma(\tau) = \langle c_\chi \rangle \cdot \frac{\iiint\limits_{-\infty}^{\infty} \mathrm{MDE}_\gamma(\vec{r}) \cdot \iiint\limits_{-\infty}^{\infty} \mathrm{MDE}_\gamma(\vec{r}') \cdot \phi_\chi(\vec{r}, \vec{r}', \tau) \ dV dV'}{\left(\iiint\limits_{-\infty}^{\infty} \mathrm{MDE}_\gamma(\vec{r}) \cdot \langle c_\chi(\vec{r}, t) \rangle \ dV \right)^2} \tag{2.35}$$

As a result, a model is introduced with a direct relation to the solution of a PDE governing the dynamics of the tracer. Now it is possible to derive the autocorrelation function for different diffusion domains.

Normal diffusion
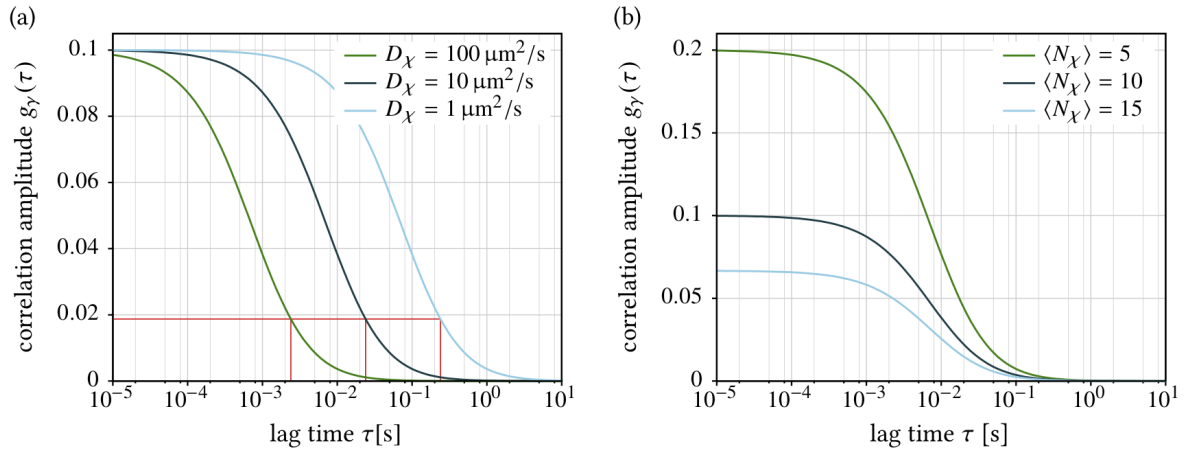
Figure 2.4: Plots of SPIM-FCS autocorrelation function for normal diffusion. In (a) the function for different diffusion coefficient is plotted and in (b) the average number of particles is varied. In (a) the red lines are representing the dwell time $\tau_{D,\chi}$ as defined in Eq. 2.30. MDE parameters: $a = 400nm$, $w_\gamma = 500$ nm, $z_\gamma = 1200$ nm. The figure is taken from [95]

The most common form of dynamics in FCS is free Brownian motion, characterised by Eq. 1.2. As it is discussed in Section 1.2, in normal diffusion, the spreading of random walker is determined by the solution to the diffusion equation 1.4. This equation can be rewritten for $c_\chi(\vec{r}, t) = \langle c_\chi \rangle + \delta c_\chi(\vec{r}, t)$ in 3-dimensions.

$$\frac{\partial \left(\langle c_\chi \rangle + \delta c_\chi(\vec{r}, t) \right)}{\partial t} = D_\chi \vec{\nabla}^2 \left(\langle c_\chi \rangle + \delta c_\chi(\vec{r}, t) \right) \quad \Rightarrow \quad \frac{\partial (\delta c_\chi(\vec{r}, t))}{\partial t} = D_\chi \vec{\nabla}^2 \delta c_\chi(\vec{r}, t), \tag{2.36}$$

where D_χ is the diffusion coefficient of species χ. The Green's function of this PDE is given by

$$P_\chi(\vec{r}, \vec{r}', \tau) = \frac{1}{(4\pi D_\chi \tau)^{3/2}} \cdot \exp\left(-\frac{(\vec{r} - \vec{r}')^2}{4 D_\chi \tau} \right), \tag{2.37}$$
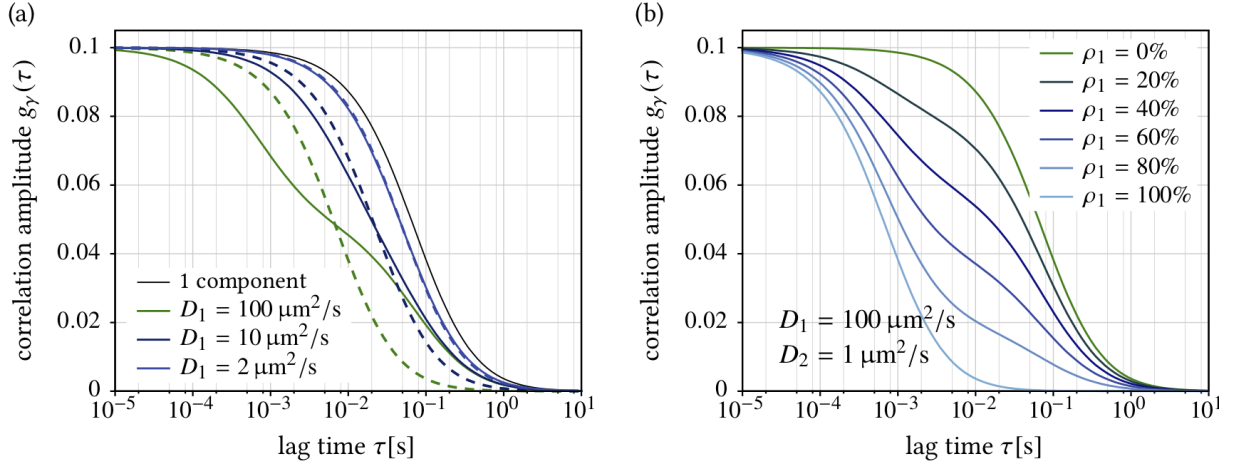
Figure 2.5: Exemplary plots of SPIM-FCS autocorrelation model for a motion with two diffusion co-
efficient. In (a) we fixed of diffusion coefficient to $D_2 = 1\,\mu m\,s^{-1}$ and D_1 is varied. The black
line is a one-component model with $\langle N1 \rangle = 10$ and $D_1 = 1\,\mu m\,s^{-1}$. The dotted lines represent
a 1-component fits to the 2-component curves. In (b) the diffusion coefficients are fixed to
$D_1 = 100\,\mu m\,s^{-1}$, $D_2 = 1\,\mu m\,s^{-1}$ in all curves, but the particle number fraction $\rho_1 := \frac{N_1}{(N_1 + N_2)}$ is
varied, keeping $N_1 + N_2 = 10$. MDE parameters: $a = 400\,nm$, $w_\gamma = 500\,nm$, $z_\gamma = 1200\,nm$. The
figure is taken from [95]

Replacing this solution in 2.35 and taking into account the Eq. 2.17 for the light sheet, the autocorrelation
function for a normal diffusion in a light sheet fluorescence microscope can be calculated.

$$G_\gamma^\chi(\tau) = \frac{\langle c_\chi \rangle}{\sqrt{\pi} z_\gamma a^2} \cdot \left\{ \mathrm{erf}\left(\frac{a}{\sqrt{4D_\chi \tau + w_\gamma^2}} \right) + \frac{\sqrt{4D\tau + w_\gamma^2}}{a \cdot \sqrt{\pi}} \cdot \left[\exp\left(-\frac{a^2}{4D_\chi \tau + w_\gamma^2} \right) - 1 \right] \right\}^2 \cdot \left(1 + \frac{4D_\chi \tau}{z_\gamma^2} \right)^{-1/2} \quad (2.38)$$

By considering Eq. 2.24 and Eq. 2.28 for MDE of a SPIM setup, we can replace the absolute concentration
with the number of fluorophores. As demonstrated in Figure 2.4(b), the autocorrelation function is
inversely proportional to the average number of fluorophores. Another important characteristics of
SPIM-FCS is the dwell time definition in Eq. 2.30. As it is evident in Figure 2.4(a), in this setup the dwell
time of a given tracer in the focus does not represent the time for the correlation function to reach its half
value $g(\tau_D) \neq g(0)/2$, anymore.

The model can also be modified to account for the possibility of particles moving with different diffusion
constants. This is a relevant presumption if we are confident about the properties of our tracer and its
behaviour in a given medium. For example if they bind to another constituent of the system or form
larger complexes that affect their motions.

Assuming that all the species have the same molecular brightness, the multi-component diffusion model
would be written in terms of an overall concentration $\langle c_{all} \rangle$ where $\langle c_{all} \rangle = \langle N_\chi \rangle / V_{eff,\gamma}$ and relative
concentration ρ_χ for each species:

$$\langle c_{all} \rangle := \sum_{\chi \in S} \langle c_\chi \rangle \qquad \rho_\chi := \frac{\langle c_\chi \rangle}{\langle c_{all} \rangle} \qquad \sum_{\chi \in S} \rho_\chi = 1 \quad (2.39)$$

In Figure 2.5 a two-component diffusion model can be seen for different combinations of diffusion
coefficients. It is visible that if the two diffusion constants are close to each other the one component

model fit (dashed line) is not clearly distinguishable and therefore it can describe the diffusion behaviour as well.

General mean squared displacement

For an abstract case of diffusion when the random motion follows an arbitrary MSD, on condition that it retains its Gaussian shape, $P_\chi(\vec{r}, \vec{r}', \tau)$ can be generalised as follow [108–111]

$$P_\chi(\vec{r}, \vec{r}', \tau) = \frac{1}{\left(2\pi \cdot \mathrm{MSD}_\chi(\tau)/3\right)^{3/2}} \cdot \exp\left(-\frac{(\vec{r} - \vec{r}')^2}{2\mathrm{MSD}_\chi(\tau)/3}\right), \tag{2.40}$$

where

$$\mathrm{MSD}_\chi(\tau) = 2d \cdot D \cdot f_\chi(\tau) \tag{2.41}$$

In this case, it is possible to prove that, for the special case of anomalous diffusion with a MSD following a power law pattern, by replacing

$$\mathrm{MSD}_\chi(\tau) = 2 \cdot d \cdot \Gamma_\chi \tau^{\alpha_\chi} \tag{2.42}$$

in Eq. 2.40, we have

$$P_\chi(\vec{r}, \vec{r}', \tau) = \frac{1}{\left(4\pi\Gamma_\chi \tau^{\alpha_\chi}\right)^{3/2}} \cdot \exp\left(-\frac{(\vec{r} - \vec{r}')^2}{4\Gamma_\chi \tau^{\alpha_\chi}}\right), \tag{2.43}$$

with the anomaly parameter α_χ and the generalised diffusion coefficient Γ_χ. This propagator can then be used like before to calculate the autocorrelation function in the case of anomalous diffusion, which is similar to Eq. 2.38, with τ replace by τ^{α_χ}

$$G_\gamma(\tau) = \frac{1}{N} \cdot \left\{ \mathrm{erf}\left(\frac{a}{\sqrt{4\Gamma\tau^\alpha + w_\gamma^2}}\right) + \frac{\sqrt{4\Gamma\tau^\alpha + w_\gamma^2}}{a \cdot \sqrt{\pi}} \cdot \left[\exp - \frac{a^2}{4\Gamma\tau^\alpha + w_\gamma^2} - 1\right] \right\}^2 \cdot \left(1 + \frac{4\Gamma\tau^\alpha}{z_\gamma^2}\right)^{-1/2} \tag{2.44}$$

Figure 2.6 shows different plots calculated for various anomaly parameters. The curves representing subdiffusive behaviour ($(\alpha_\chi < 1)$) are flatter compared the normal diffusion case ($\alpha_\chi = 1$) and they span larger range in time whereas superdiffusion ($\alpha_\chi = 1.5$) curve exhibits a sharper decay. This effect was anticipated from the theory of anomalous diffusion and the resulting patters of motion.

It is now possible to extract important dynamical characteristics of the system from its experimentally derived autocorrelation function in a light sheet microscopy setup. In this study, we have used the optical setup designed and assembled in our lab. All the information regarding the setup is summarised in Krieger et al. [95, 112].
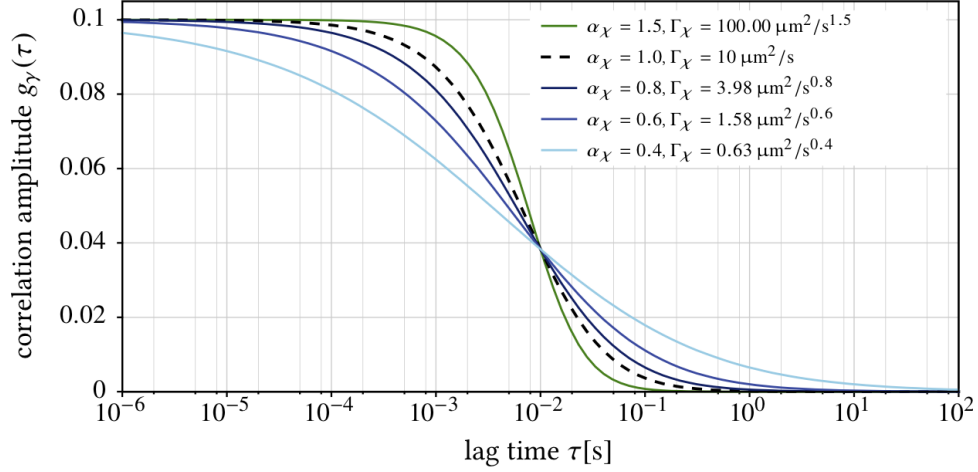
Figure 2.6: Sample curve calculated from SPIM-FCS autocorrelation function for anomalous diffusion. The value for the generalised diffusion coefficient parameter $\Gamma_\chi = 10\,\mu m\,s^{-\alpha}$ is chosen for the curves to coincide at a $\tau = 10$ ms. MDE parameters: $a = 400nm$, $w_\gamma = 500$ nm, $z_\gamma = 1200$ nm. The figure is taken from [95]

2.4 Fluorescence cross-correlation spectroscopy

The theory of fluorescence correlation spectroscopy has been further extended to measure the co-mobility and possible binding reactions between two molecular species by tagging each of them with a different fluorescent marker. Moreover, spatial correlations are integrated in the fluctuations of fluorescent signals as these fluctuations are indicative of the motion in a certain time. Using this technique we can explore the heterogeneities in the distribution, dynamics and interactions of our sample system. Both extensions can be incorporated in an imaging setup with a fast detector as is capable of recording the intensity profiles both in space and time. Analysis of these fast image series can be done by defining a cross correlation function at two different points in space or between particles carrying spectrally distinct fluorophores.

For this reason, let us define a generalised cross-correlation function to account for the fluctuation of two fluorescence signal at spatially apart positions:

$$g_{\gamma\varrho}(\vec{\xi},\tau) = \frac{\left\langle \delta F_\gamma(\vec{r},t) \cdot \delta F_\varrho(\vec{r}+\vec{\xi},t+\tau) \right\rangle}{\left\langle F_\gamma(\vec{r};t) \right\rangle \cdot \left\langle F_\varrho(\vec{r};t) \right\rangle} \tag{2.45}$$

Note that autocorrelation function therefore is a special case of Eq. 2.45 when the indices are the same ($g_{\gamma\gamma}$ or $g_{\varrho\varrho}$) and $\vec{\xi} = 0$.

$g_{\gamma\varrho}(\vec{\xi},\tau)$ can be rewritten in an explicit generalised form for $G_{\gamma\varrho}^\chi(\vec{\xi},\tau)$

$$g_{\gamma\varrho}(\vec{\xi},\tau) = \frac{\sum\limits_{\chi\in\mathbb{S}} \eta_{\gamma,\chi}\eta_{\varrho,\chi} G_{\gamma\varrho}^\chi(\vec{\xi},\tau)}{\left(\sum\limits_{\chi\in\mathbb{S}} \eta_{\gamma,\chi}\left\langle c_\chi \right\rangle\right) \cdot \left(\sum\limits_{\chi\in\mathbb{S}} \eta_{\varrho,\chi}\left\langle c_\chi \right\rangle\right)}, \tag{2.46}$$

and accordingly we will define non-normalised correlation function

$$G_{\gamma\varrho}^{\chi}(\vec{\xi},\tau) = \langle c_{\chi} \rangle \cdot \frac{\iiint\limits_{-\infty}^{\infty} \iiint\limits_{-\infty}^{\infty} \mathrm{MDE}_{\gamma}(\vec{r}) \cdot \mathrm{MDE}_{\varrho}(\vec{r}') \cdot \phi_{\chi}(\vec{r},\vec{r}',\tau) \; dV \, dV'}{\left(\iiint\limits_{-\infty}^{\infty} \mathrm{MDE}_{\gamma}(\vec{r}) \cdot \langle c_{\chi}(\vec{r},t) \rangle \; dV \right) \cdot \left(\iiint\limits_{-\infty}^{\infty} \mathrm{MDE}_{\varrho}(\vec{r}) \cdot \langle c_{\chi}(\vec{r},t) \rangle \; dV \right)} \tag{2.47}$$

where $\vec{r}$ is a function of $\vec{\xi}$. Now we can calculate the appropriate cross-correlation function for different scenarios.

Spatial cross-correlation function

In this case, two observation volumes that are displaced by $\vec{\delta} = (\delta_x, \delta_y, \delta_z)$ are taken into account (see Figure 2.7). Assuming, without loss of generality, that there is a flow from the first focal volume (left) to the second one (right) with the flow velocity $\|\vec{v}\|$. Then, the fluorescence intensity traces detected from the left focus can be tracked in the right one after a delay. This delay is the time needed for the particle to travel from the left focus to the right one by the flow and it can be characterised by $\tau_F = \|\vec{\delta}\| / \|\vec{v}\|$. This can be translated to a cross-correlation function based on Eq. 2.47 with certain assumptions. As the same illumination intensity, detection filters and optical detectors are used for both foci, the molecular brightnesses can be expected to be the same. So the MDEs have the same size with a shift $\|\vec{\delta}\|$. (Note that the indices γ and ϱ represent two foci, in this case)

$$\eta_{\gamma,\chi} = \eta_{\varrho,\chi} \quad \text{and} \quad \mathrm{MDE}_{\gamma}(\vec{r}) = \mathrm{MDE}_{\varrho}(\vec{r} + \vec{\delta}) \quad \text{or} \quad \mathrm{MDE}_{\varrho}(\vec{r}) = \mathrm{MDE}_{\gamma}(\vec{r} - \vec{\delta}) \tag{2.48}$$

Hence, we can explicitly calculate the spatial cross-correlation function for a SPIM-FCS setup under these assumptions. This function can be written in terms of three direction factors $G_{\gamma\varrho}^{\chi}(\vec{\xi},\tau) = \langle c_{\chi} \rangle \cdot G_{\gamma\varrho,x}^{\chi}(\vec{\xi},\tau) \cdot G_{\gamma\varrho,y}^{\chi}(\vec{\xi},\tau) \cdot G_{\gamma\varrho,z}^{\chi}(\vec{\xi},\tau)$ where the factors along x- and y- direction are equal.

$$\begin{aligned}
G_{\gamma\varrho,x}^{\chi}(\vec{\xi},\tau) = \frac{1}{2a^2} \cdot \Bigg\{ & \Bigg[(a - v_x\tau + \delta_x) \cdot \mathrm{erf}\left(\frac{a - v_x\tau + \delta_x}{\sqrt{4D_{\chi}\tau + w_{\gamma}^2}} \right) - 2(v_x\tau - \delta_x) \cdot \mathrm{erf}\left(\frac{v_x\tau - \delta_x}{\sqrt{4D_{\chi}\tau + w_{\gamma}^2}} \right) \\
& + (a^2 + v_x\tau - \delta_x) \cdot \mathrm{erf}\left(\frac{a + v_x - \delta_x}{\sqrt{4D_{\chi}\tau + w_{\gamma}^2}} \right) \Bigg] + \frac{\sqrt{4D_{\chi}\tau + w_{\gamma}^2}}{\sqrt{\pi}} \cdot \Bigg[\exp\left(-\frac{(a - v_x\tau + \delta_x)^2}{4D_{\chi}\tau + w_{\gamma}^2} \right) \\
& - 2 \cdot \exp\left(-\frac{(v_x\tau - \delta_x)^2}{4D_{\chi}\tau + w_{\gamma}^2} \right) + \exp\left(-\frac{(a + v_x\tau - \delta_x)^2}{4D_{\chi}\tau + w_{\gamma}^2} \right) \Bigg] \Bigg\},
\end{aligned} \tag{2.49}$$

and the expression in z- dircetion is

$$G_{\gamma\varrho,z}^{\chi}(\vec{\xi},\tau) = \frac{\exp\left(-\frac{(v_z\tau - \delta_z)^2}{4D_{\chi}\tau + z_{\gamma}^2} \right)}{\sqrt{\pi} \cdot \sqrt{4D_{\chi}\tau + z_{\gamma}^2}}. \tag{2.50}$$

As we are studying a system in equilibrium, we will be mostly concerned with the scenario where no flow in the sample is present. In this case, as well, we will see a peak in the spatial cross correlation curve if the distance between two foci is large enough. The peak is denoting the time that the particle requires to cover the distance between two foci only through its random motion.
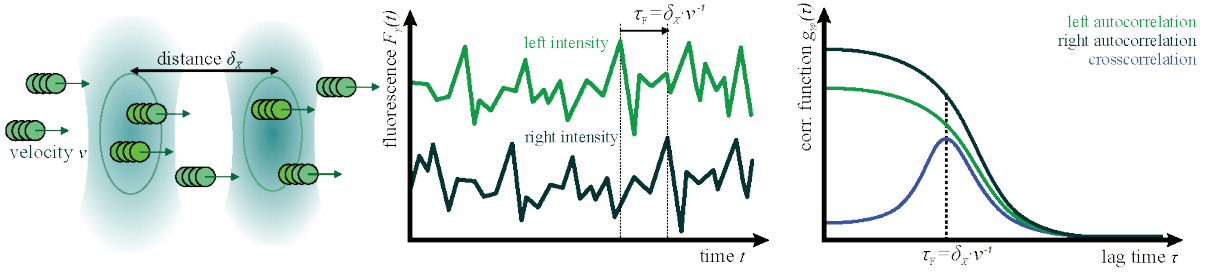
Figure 2.7: Graphical explanation of spatial cross correlation between two foci. Particles moving from left to right through two foci separated by a distance $\vec{\delta}$. The flow velocity is v. The intensity traces are shifted by a time τ_{F_χ}. The cross correlation function shows a pick at this time. The figure is taken from [95]

Two-color cross-correlation function

To characterise the interaction between two particles, tagged with two spectrally appropriate fluorophores, we should utilise another type of correlation analysis, termed two-color fluorescence cross-correlation spectroscopy (FCCS). This type of cross-correlation analysis is performed between two different fluorescence intensities F_γ and F_ϱ at two overlapping focal planes. For the fluorescent dyes to be compatible for this technique, they have to belong to two distinct spectral ranges. Otherwise, the detector is not able to differentiate them.

Figure 2.8 shows a schematic of this technique for diffusers tagged with green fluorescence(F_g) and red (F_r) fluorescence. If there is an interaction between these two kinds of particles, they are going to move together (depicted as dimers in Figure 2.8). This co-mobility will cause a correlation between these two distinct fluorescence signals. The amplitude of this correlation function $g_{\gamma\varrho}(0)$ reveals the presence of an interaction. As a result, if there is no co-mobility, the two signals are statistically independent from each other and the cross-correlation amplitude is zero. Moreover, if we tag two types of molecules A and B then the $g_{\gamma\varrho}(0)$ depends on the concentration of the complex formed as a result of their interaction or $C_{AB}/(C_A + C_B)$. Theoretically, in the case of full interaction, this relative concentration will be approximately the average between the respective autocorrelation function amplitudes ($g_{\gamma\gamma}(0)$ and $g_{\varrho\varrho}(0)$).

It is once more possible to adapt the same approach as presented in spatial cross correlation analysis. To do so, we need to reconsider our assumptions in 2.48. In this case, MDEs may be different. The shift $\vec{\delta}$ is retained in the model though. This is due to chromatic aberrations and the possibility of optical misalignment that will ultimately lead to an offset $\vec{\delta}$ between the two foci.

The prior information on spectral properties of both fluorophores, as well as the expected interaction between them help us to define new constraints for the molecular brightness of the species $\xi \in \{A, B, AB\}$. Considering the simplest model of interaction between the species $A + B \rightleftharpoons AB$ and assuming that A is labeled by a fluorescence label (denoted by the index γ) with a lower wavelength compared to B (denoted by the index ϱ), we can formulate the following assumptions on the molecular brightness

$$\begin{aligned} \eta_{\gamma,A} &\equiv \eta_\gamma & \eta_{\gamma,B} &= 0 & \eta_{\gamma,AB} &\equiv \eta_\gamma \\ \eta_{\varrho,A} &= \kappa_{\gamma\varrho}\eta_\gamma & \eta_{\varrho,B} &\equiv \eta_\varrho & \eta_{\varrho,AB} &= \eta_\varrho + \kappa_{\gamma\varrho}\eta_\gamma \end{aligned} \tag{2.51}$$

where the $\kappa_{\gamma\varrho}$ denotes the crosstalk between channel γ and ϱ *i.e.* the fraction of γ fluorescence which is detected in the ϱ channel because of the broad emission spectra (Figure 2.9) and imperfect filters. It can
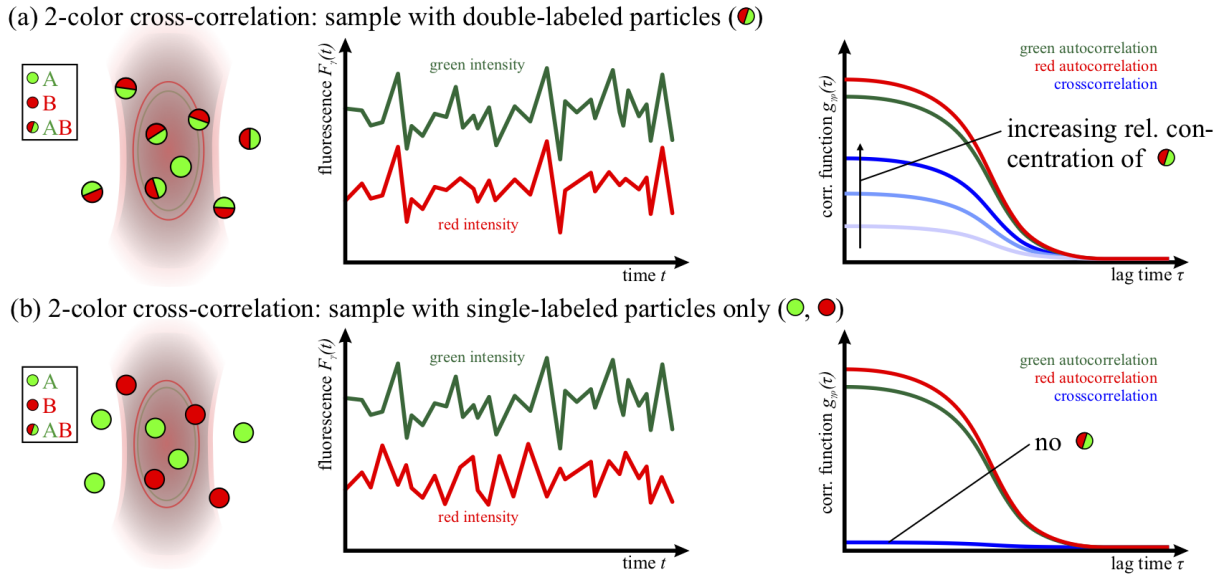
Figure 2.8: Sketch of two-color fluorescence cross correlation spectroscopy. (a) Many double-labeled particles are moving together and as a result there is a high cross-correlation amplitude. In (b) most of the particles are moving independently from each other resulting in almost zero cross-correlation amplitude. The figure is taken from [95]

be calculated as

$$
\kappa_{\gamma\varrho} = \frac{\int\limits_0^\infty \eta_\gamma(\lambda) \cdot h_\varrho(\lambda) \; d\lambda}{\int\limits_0^\infty \eta_\gamma(\lambda) \; d\lambda}
\tag{2.52}
$$

in which $h_\varrho(\lambda)$ is the transmission spectrum of the ϱ detection channel. Figure 2.9 shows the absorption and emission spectra for three popular fluorescent proteins in multiple-channel microscopy techniques. Crosstalk can be seen where there is an overlap between the excitation spectrum and the detection channel. As an example, if the longpass filter in the red channel starts transmitting at 600 nm, the crosstalk for eGFP at the red channel is $\kappa_{gr} \approx 0.38$ [95].
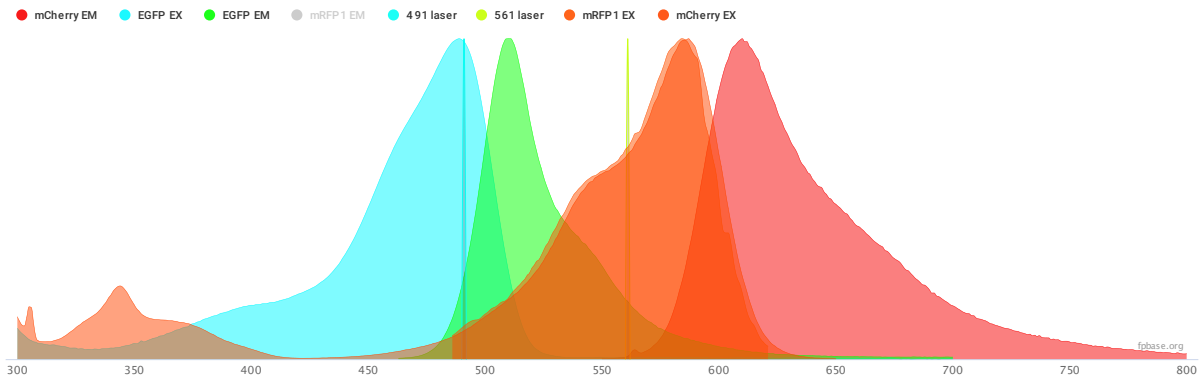
Figure 2.9: Absorption and fluorescence spectra of typical fluorescence proteins used in FC(C)S. The x-axis presents the wavelength (λ[nm] The figure is generated from the website introduced at [113]

The molecular brightness can be estimated from the average fluorescence intensities $\langle F_\gamma \rangle$ and $\langle F_\varrho \rangle$ and the concentration of species χ in the focal volume.

$$\eta_\gamma = \frac{\langle F_\gamma \rangle}{\langle c_A \rangle + \langle c_{AB} \rangle} \qquad \text{and} \qquad \eta_\varrho = \frac{\langle F_\varrho \rangle}{\langle c_A \rangle + \langle c_{AB} \rangle} \tag{2.53}$$

The cross-correlation function for two-colour FCCS can be calculated using the relation for the general cross-corelation function (2.46) and the constraints introduced in Eq. 2.51 as follow

$$g_{\gamma\gamma} = \frac{\eta_\gamma^2 \, G_{\gamma\gamma}^A(\tau) + \eta_\gamma^2 \, G_{\gamma\gamma}^{AB}(\tau)}{\eta_\gamma^2 \cdot (\langle c_A \rangle + \langle c_{AB} \rangle)^2} \tag{2.54}$$

$$g_{\varrho\varrho} = \frac{\eta_\varrho^2 \cdot \left(G_{\varrho\varrho}^B(\tau) + G_{\varrho\varrho}^{AB}(\tau) \right) + \kappa_{\gamma\varrho}^2 \, \eta_\gamma^2 \, \left(G_{\gamma\gamma}^A(\tau) + G_{\gamma\gamma}^{AB}(\tau) \right) + 2\kappa_{\gamma\varrho} \, \eta_\varrho \, \eta_\gamma \, G_{\gamma\varrho}^{AB}(\tau)}{\left(\kappa_{\gamma\varrho} \, \eta_\gamma \cdot \langle c_A \rangle + (\eta_\varrho + \kappa_{\gamma\varrho} \, \eta_\gamma) \cdot \langle c_{AB} \rangle + \eta_\varrho \, \langle c_B \rangle \right)^2} \tag{2.55}$$

$$g_{\gamma\varrho} = \frac{\eta_\gamma \, \eta_\varrho \, G_{\gamma\varrho}^{AB}(\tau) + \kappa_{\gamma\varrho} \, \eta_\gamma \, \eta_\varrho \, G_{\gamma\varrho}^A(\tau) + \kappa_{\gamma\varrho} \, \eta_\gamma^2 \, G_{\gamma\gamma}^{AB}(\tau)}{\left(\eta_\gamma \, \langle c_A \rangle + \eta_\gamma \, \langle c_{AB} \rangle \right) \cdot \left(\kappa_{\gamma\varrho} \, \eta_\gamma \cdot \langle c_A \rangle + (\eta_\varrho + \kappa_{\gamma\varrho} \, \eta_\gamma) \cdot \langle c_{AB} \rangle + \eta_\varrho \, \langle c_B \rangle \right)} \tag{2.56}$$

The non-normalised cross-correlation function has a similar form as the one in the previous section (Eq. 2.49 and Eq. 2.50). The difference is in altered MDE parameters since the PSF is dependant on the wavelength of the fluorescence signal *i.e.* we have two different widths w_γ and w_ϱ and heights z_γ and z_ϱ. Therefore for two-colour SPIM-FCCS, the non-normalised cross correlation at each coordinate direction (equal factors at x- and y-direction) can be written as

$$\begin{aligned} G_{\gamma\varrho,x}^\chi(\vec{\xi},\tau) = \frac{1}{2a^2} \cdot &\left\{ \left[(a - v_x\tau + \delta_x) \cdot \text{erf}\left(\frac{\sqrt{2} \cdot (a - v_x\tau + \delta_x)}{\sqrt{8D_\chi\tau + w_\gamma^2 + w_\varrho^2}} \right) - 2(v_x\tau - \delta_x) \cdot \text{erf}\left(\frac{\sqrt{2} \cdot (v_x\tau - \delta_x)}{\sqrt{8D_\chi\tau + w_\gamma^2 + w_\varrho^2}} \right) \right. \right. \\ &+ (a^2 + v_x\tau - \delta_x) \cdot \text{erf}\left(\frac{\sqrt{2} \cdot (a + v_x - \delta_x)}{\sqrt{8D_\chi\tau + w_\gamma^2 + w_\varrho^2}} \right) \Bigg] + \frac{\sqrt{8D_\chi\tau + w_\gamma^2 + w_\varrho^2}}{\sqrt{2\pi}} \\ &\cdot \left[\exp\left(-\frac{2 \cdot (a - v_x\tau + \delta_x)^2}{8D_\chi\tau + w_\gamma^2 + w_\varrho^2} \right) - 2 \cdot \exp\left(-\frac{2 \cdot (v_x\tau - \delta_x)^2}{8D_\chi\tau + w_\gamma^2 + w_\varrho^2} \right) + \exp\left(-\frac{2 \cdot (a + v_x\tau + \delta_x)^2}{8D_\chi\tau + w_\gamma^2 + w_\varrho^2} \right) \right] \Bigg\}, \end{aligned} \tag{2.57}$$

and along z-direction, it will be

$$G_{\gamma\varrho,z}^\chi(\tau) = \sqrt{\frac{2}{\pi}} \cdot \frac{\exp\left(-\frac{2 \, (v_z\tau - \delta_z)^2}{8D_\chi\tau + z_\gamma^2 + z_\varrho^2} \right)}{\sqrt{\pi} \cdot \sqrt{8D_\chi\tau + z_\gamma^2 + z_\varrho^2}}. \tag{2.58}$$

In all the expressions for the cross-correlation function, it is possible to replace the normal diffusion assumption with the anomalous diffusion following a power-law pattern. As in Section 2.3 (FCS theory for different types of diffusion), it suffices to replace $D_\chi\tau$ by $\Gamma_\chi\tau^\alpha$. We can similarly introduce multi-component diffusion by exploiting Eq. 2.39 for two or more cross-correlation functions.

RESULTS

3 Chromatin and A-type lamins interdependence

As it has been discussed in Chapter 1, the presence of nucleoplasmic lamins as a highly dynamic pool and their function in the nucleus and nucleoskeleton has been a subject of interest for molecular biologists. Especially since it was found that these non-lamina-binding lamins in the nucleus are not a transient pool before their assembly into the lamina [114]. On the other hand, the view on the chromatin, its rearrangement and its dynamics is constantly evolving and new findings emphasise the need for more quantifiable, interdisciplinary studies. Besides biology, the very exotic nature of the cell nucleus for physicists and its viscoelastic properties naturally engage the attention of exact scientists involved with the study of complex systems. This is what we took into consideration in this thesis by investigating the chromatin mobility and its dependence on A-type nucleoplasmic lamins.

In this chapter the results of our FC(C)S studies on the histone mobility will be presented. Histones together with DNA wound around them at the first stage of compaction, make up the nucleosomes which are the basic units of chromatin fibre. Therefore inspecting their random motion gives us an insight on the chromatin dynamics. For this study we used the following cell lines:

- ▶ Mouse adult fibroblasts adherent cells (MAF) as wildtypes. They stably express H2A-eGFP
- ▶ Lamin A/C knockout mouse adult fibroblasts [115] (LMNA$^{-/-}$ MAF-H2A-mRFP) stably expressing H2A-mRFP
- ▶ Lamin A/C knockout mouse adult fibroblasts (LMNA$^{-/-}$ MAF-H2A-eGFP) stably expressing H2A-eGFP

First chromatin interconnections with intranuclear lamin As will be examined in Section 3.1 , then random motions of chromatin in the presence and absence of nucleoplasmic A-type lamins in Section 3.2 will be studied and finally we will consider the dependance of chromatin's spatial rearrangements on A-type lamins in the nuclear interior in the last section of this chapter.

3.1 Lamin A interconnections

We applied SPIM-FCCS to investigate how lamin A interacts with chromatin, using our lamin A knockout mouse adult fibroblast cell line stably transfected with H2A-mRFP1 (LMNA$^{-/-}$ MAF-H2A-mRFP), then transiently co-transfected with lamin A-eGFP. The replacement of endogenous lamin A proteins with fluorescently labeled ones enables us to study the co-mobility between lamin A and histones. The cells were either grown on small cover slides or embedded in 2% agarose gels in order to halt cellular movement. Cells selected for measurements showed a healthy shape (no blebs, a recognisable nucleus, typical flattened shape) and were not obviously in mitosis. For each condition, several cells were acquired on different days. Cells that moved during the measurements, in which the bleach correction did not succeed because of slow large-scale fluctuations, or that showed other unusual artefacts (*e.g.* large internal rearrangements, aggregates) were excluded. This way ≈30% of the cells were removed from further evaluations. To reduce cell movements, all measurements were performed at room temperature (24 °C). The measurements on cover slides and in gels were cross-validated and prove to be mutually consistent (see Table 3.1). For better statistics, $2 * 2$ pixel binning was used on the image series. For the sake of brevity, we refer to $2 * 2$ binned pixels as pixel in this chapter unless otherwise is mentioned.

As negative control, we transiently transfected LMNA$^{-/-}$ MAF-H2A-mRFP with eGFP tetramer(eGFP-4x), which does not interact with chromatin and should therefore show only negligible cross-correlation (CC). Figure 3.1 displays auto- and cross-correlation curves for a sample cell (upper panel) and a control (lower

	Cover slips		2% agarose gel	
	control	sample	control	sample
q	0.01 ± 0.07	0.36 ± 0.34	0.00 ± 0.06	0.31 ± 0.18

Table 3.1: Statistical overview of the relative cross correlation function amplitude q over measured cells on cover slips and embedded in 2% agarose gel. The gels were made of phenol-red free HBSS. Control cells are LMNA$^{-/-}$ MAFs transiently expressing eGFP4x and as sample cells, we used LMNA$^{-/-}$ MAFs transintly expressing lamin A-eGFP.

panel). The amplitude of CC of the control is not larger than the crosstalk indicated by the horizontal dashed line. In the sample cell, the nonzero ACF amplitude demonstrates that the dynamics of both lamin A and histones have a stochastic character and the nonzero CC demonstrates that lamin A and histones are diffusing together and indicates that there is a form of interconnection between the two species. We also notice that the decay of the two autocorrelation functions is very similar, indicating a similar diffusive motion of the two species.
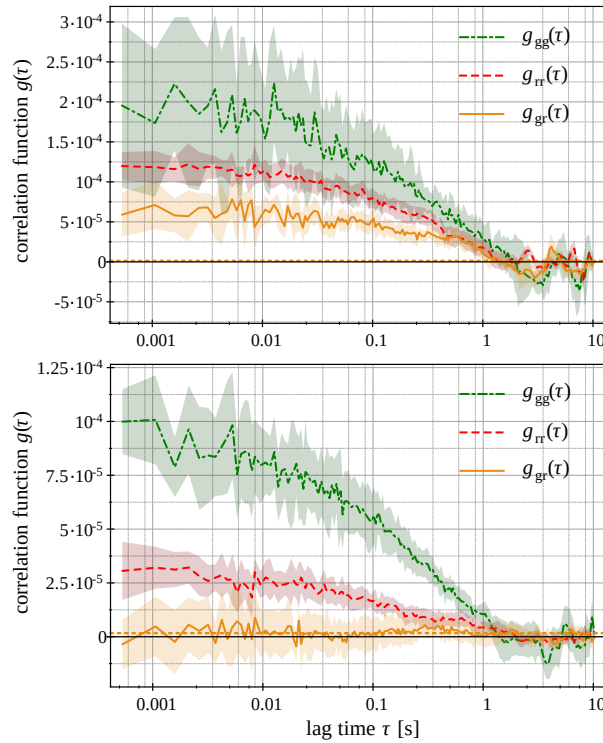
Figure 3.1: Examples of typical auto-(green/red) and cross-correlation(orange) curves (solid lines are the averages and the shadowed polygons show the standard deviation of the correlation function calculated at each pixel). The upper panel shows the average cross-correlation and standard deviation of laminA-eGFP with H2A-mRFP together with their respective auto-correlation functions corresponding to one non-binned pixel selected in a sample cell. The lower panel reports the cross-correlation function and the standard deviation of eGFP4x with H2A-mRFP next to auto-correlation functions of each of them at a selected single pixel (a $1*1$ pixel) of a control cell. Both sample cells and controls are LMNA$^{-/-}$/ MAF-H2A-mRFP transiently transfected with lamin A-eGFP and GFP-4x respectively. The horizontal dashed line indicates the cross-talk level between green and red channels.

To quantify the interaction between lamin A and histone proteins, the relative cross-correlation function

(CCF) amplitude was calculated for all pixels of each acquisition. For this reason, first a 2-component normal diffusion model was fitted to the auto-correlation curves of all different pixels in image series for each channel. The quicker ones represent the freely moving histones or lamin A-s, whereas the slower diffusion means binding to a larger structure e.g. chromatin. Then the cross-correlation curves corresponding to each pixel were fitted with a single-component normal diffusion model where w_γ and z_γ have been replaced, since the signals were collected over different spectral bands, with slightly different optical resolution. Therefore, in order to fit the cross-correlation function with a single component model and retrieve a diffusion coefficient, we assume an average value of the optical resolution. Since the dwell time is linearly proportional to the square of the linear size of the observation volume, we recalculate the resolution in the sample plane and along the optical axis as:

$$w = \sqrt{\frac{w_g^2 + w_r^2}{2}} \quad , \quad z = \sqrt{\frac{z_g^2 + z_r^2}{2}} \tag{3.1}$$

Finally the amplitude of each model ($g_{\gamma\rho}(0)$) was extracted. Relative CCF amplitude then is defined as:

$$q = \frac{g_{gr}(0)}{min(g_{gg}(0), g_{rr}(0))} \tag{3.2}$$

In this equation (eq. 3.2) we are considering on equal foot lamin A proteins and histones and evaluating the number of less abundant objects that are co-diffusing with the more abundant ones. Figure 3.2 shows a representative map of the relative CCF amplitude (q) obtained from a cell expressing laminA-eGFP and H2A-mRFP.
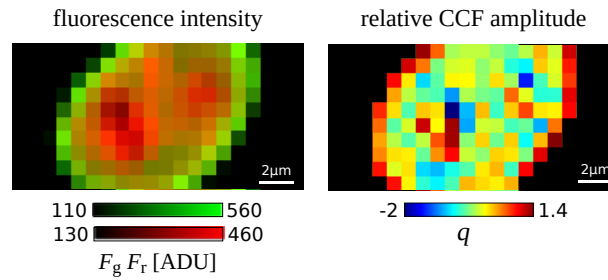
Figure 3.2: Parameter images of SPIM-FCCS measurement of lamin A-eGFP and H2A-mRFP. The distribution of the lamin A (green) and the H2A (red) fluorescence signals can be seen in the left panel (Analogue-to-Digital converter unit [ADU] is the output unit of EMCCD camera). The map of the relative CCF amplitude in the nucleus of LMNA$^{-/-}$ MAF-H2A-mRFP transiently transfected with lamin A-eGFP is shown in the right panel. Negative values of q are originated by the instrumental noise.

Figure 3.3 summaries the relative FCCS amplitude over all measured cells. These results demonstrate that a considerable fraction (more than 30%) of lamin A is co-diffusing with histone proteins. A one-component normal diffusion fit to the CCF, averaged over all pixels in the cell, yields a diffusion coefficient $D_{CCF} = 0.33 \pm 0.18 \mu m^2/s$ on cover slips and $D_{CCF} = 0.33 \pm 0.2 \mu m^2/s$ for the cells embedded in agarose gels, compatible with the slow component of the histone motion (Table 3.2). This suggests that lamin A is associated to chromatin-bound histones only.
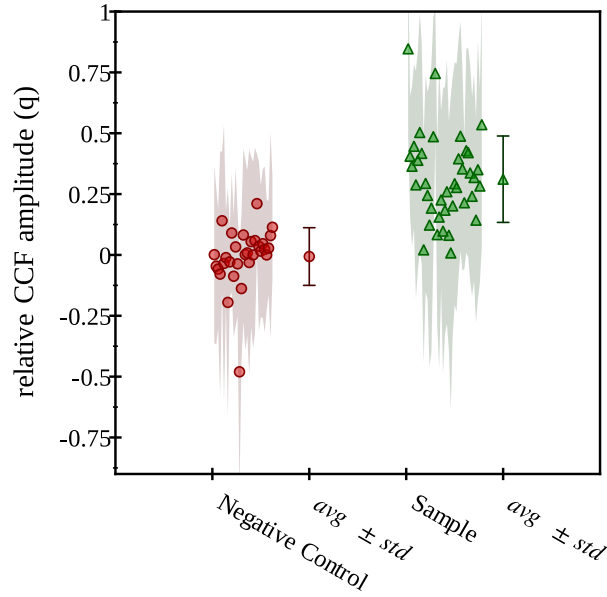
Figure 3.3: Statistical summary of the relative FCCS amplitude in LMNA$^{-/-}$ MAF-H2A-mRFP expressing eGFP4x, as negative control, and Lamin A-eGFP using SPIM-FCCS. The medians of the relative FCCS amplitudes for 31 negative control cells are pooled together and shown by small filled circles. For 39 sample cells, the medians are displayed as small filled triangles. The average and standard deviation of these medians can be found next to them as a filled circle with error bars for negative control and filled triangle with error bars for sample.

3.2 Alterations in the diffusivity of histones

As we have shown in Section 3.1, there exists a form of comobility between A-type lamins and chromatin that manifests itself in a non zero cross correlation amplitude. In this section we explored the possible effects of this interaction on the diffusional behaviour of histones. For this reason, we employed SPIM-FCS to characterise random motions of H2A in the presence and absence of A-type lamins.
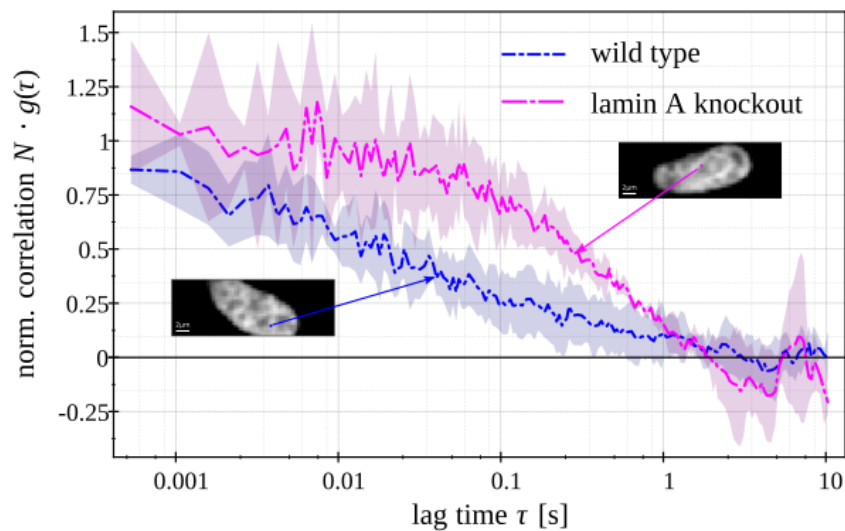
Figure 3.4: Typical FCS auto-correlation functions taken at the single pixels, as indicated in the corresponding SPIM images of the MAF wild type and lamin A knockout cells.

	MAF	LMNA$^{-/-}$ MAF
α	0.83 ± 0.08	1.11 ± 0.10
τ_Γ [ms]	641 ± 170	1158 ± 238
D_{fast} [$\mu m^2/s$]	24.5 ± 4.8	32.1 ± 8.3
D_{slow} [$\mu m^2/s$]	0.28 ± 0.05	0.24 ± 0.04
ρ_{slow}	0.46 ± 0.09	0.66 ± 0.09

Table 3.2: Averages and standard deviation of the fit parameters over the whole sample of cells that express H2A-eGFP (75 MAFs and 75 LMNA$^{-/-}$ MAF). The parameters in the first two rows are the result of anomalous diffusion fit model and the rest are obtained from 2-component normal diffusion fit model

Figure 3.4 shows the fluorescent intensity images of a wild type cell and a lamin A knockout cell, both expressing H2A-eGFP, together with two typical auto-correlation curves at the single pixels ($1 * 1$ pixels) highlighted in the fluorescence images. A clear effect is evident by comparing the curves. Contrary to the curve in the lamin A knockout cell, the auto-correlation curve in the wildtype demonstrates a shorter correlation time and its overall shape is substantially different. To describe this effect two different SPIM-FCS models were fitted to the auto-correlation curves (eq. 2.2): an anomalous diffusion model (Eq. 2.44) assuming the diffusion is anomalous and the fraction of freely diffusing particles and internal chromatin dynamics are negligible and a 2-component normal diffusion model (Eq. 2.38) in which the diffusion is normal and we are expecting two different diffusing particles. The slower ones are assumed to be chromatin-bound histones and the faster ones can account for either unbound histones or faster internal dynamics of chromatin. Figure 3.5 shows typical fits for both models, which do not differ significantly in fit quality. Thus, these are more or less equally valid ways to account for the crowded environment in live cells.
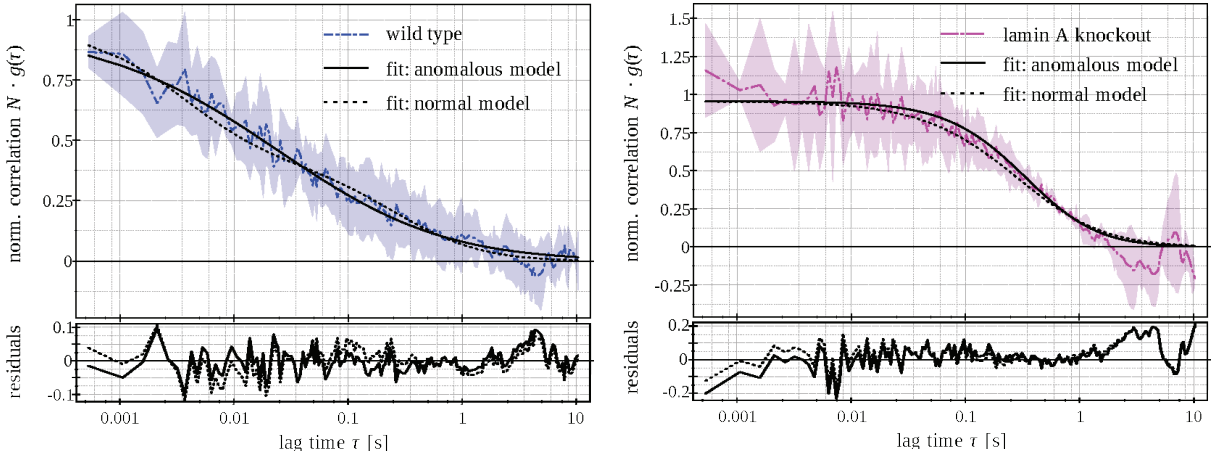
Figure 3.5: FCS auto-correlation functions against different fit models and their corresponding residuals. auto-correlation curves, two different fits and residuals calculated at non-binned pixels in fluorescence image series acquired from MAF cells expressing H2A-eGFP as wild type (upper panel) and LMNA$^{-/-}$ MAF cells expressing H2A-eGFP (lower panel)

The 2-component normal diffusion model has four fit parameters (number of particles in a focal volume N, fast diffusion coefficient D_{fast}, slow diffusion coefficient D_{slow} and the fraction of particles diffusing slowly ρ_{slow}), whereas the anomalous diffusion model has only three (number of particles in a focus N, anomaly parameter α and anomalous diffusion coefficient Γ). For the two-component normal diffusion fit, the fast diffusion coefficient was fixed to ensure a better convergence of the algorithm. This fast component is usually interpreted as the diffusion coefficient of free histones, and it is in the same range

as those obtained for inert tracer proteins [116, 117]. The slow component corresponded to the motion of chromatin-bound histones. For all pixels in each cell image series, a 2-component normal diffusion fit with all parameters free is performed and the median of the D_{fast} distribution is calculated. Then this value is fixed and the auto-correlation curve of each pixel is fitted again with the same model.
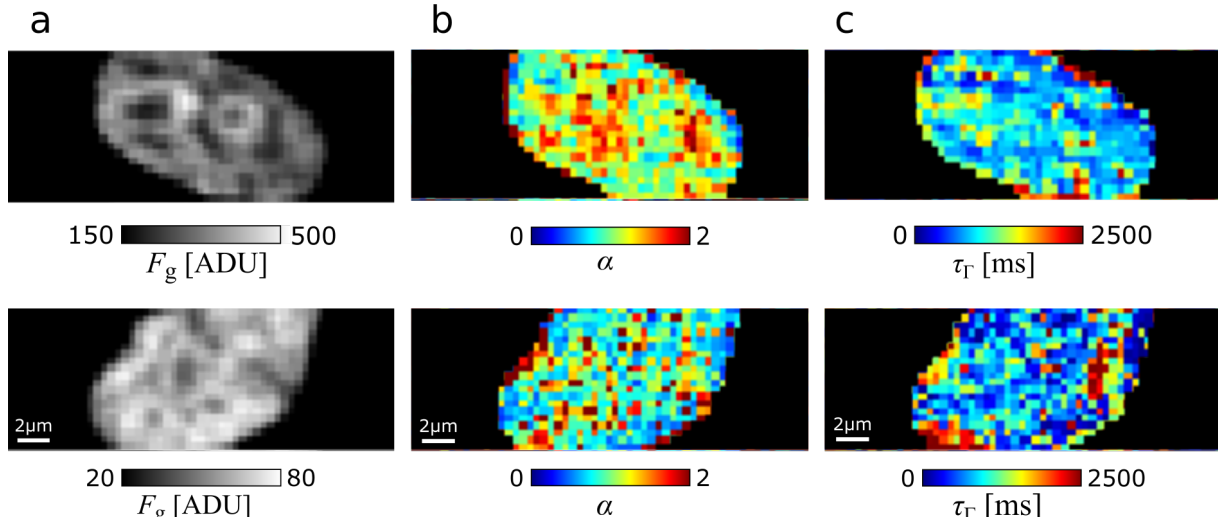
Figure 3.6: Maps of fluorescence intensity, diffusion anomaly and dwell time in a LMNA$^{-/-}$ MAF (upper row) and MAF wildtype (lower row). (a) Fluorescence intensity images of a LMNA$^{-/-}$ MAF and MAF wildtype expressing H2A-eGFP represented in Analogue-to-Digital converter unit [ADU] which is the output unit of EMCCD camera. For each cell, (b) the map of anomaly parameter α and (c) dwell time τ_Γ, obtained from the anomalous diffusion model, are shown in their corresponding column.

Figure 3.5 show fluorescence images and fit results for a typical wild type and a lamin A knockout cell expressing H2A-eGFP. The good result of the fitting procedure indicates that the fluctuations can be described by a random motion statistics. Since a random motion in cell can be defined as the motion whose correlation function (measured on a signal collected through a high numerical aperture objective lens) is described by a hyperbolic decay. From the anomaly parameter maps (Figure 3.6), it is visually apparent that histone diffusion is more anomalous in the wild type than in the lamin A knockout cells. Moreover, the fraction of the slow component in the 2-component normal diffusion fit increases for the knockout cells (Table 3.2).

In most cases, the histograms of the fit parameters over all the pixels of the same cell contain a certain number of outliers and often feature broad distributions. Therefore, robust statistical estimators, such as the median, are used for any further evaluation. Figure 3.7 summarizes the fit results for the anomaly parameter and dwell time of all pixels in all measured cell nuclei (160 MAFs and 153 LMNA$^{-/-}$ MAFs).

The statistical averages over all pixels in all cells confirm that histone mobility in the wildtype fibroblasts is well described by anomalous subdiffusion ($\alpha = 0.83 \pm 0.08$). In MAFs lacking A-type lamins, the anomaly of this motion is no longer observed and a normal diffusion model is enough to explain the data ($\alpha = 1.11 \pm 0.10$). These results agree with the recent findings about telomere motion [118]. Furthermore, we detect a significant slowing down of histone mobility when lamin A is missing, indicated by an increased dwell time. Similar conclusion can be reached from the two-component model as the fraction of slow component increases when passing from the wild type cells ($\rho_{slow} = 0.46 \pm 0.09$) to the lamin A knockout ones ($\rho_{slow} = 0.66 \pm 0.09$).

(a)   (b)
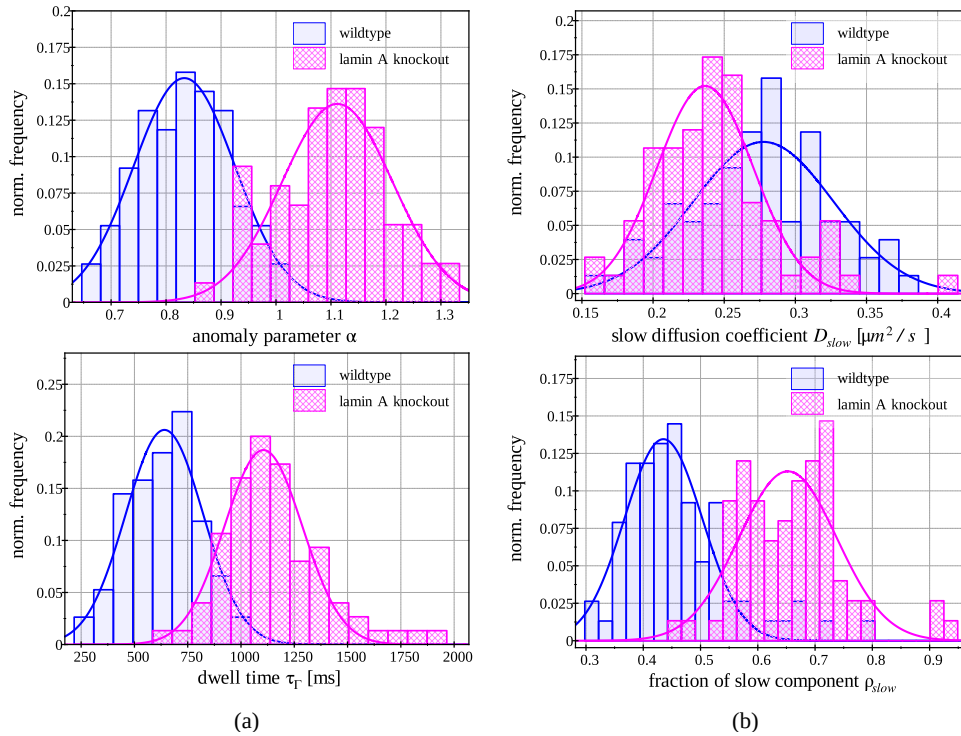
Figure 3.7: The distributions of fit parameters over all measured cells: (a) Fit results obtained with the anomalous diffusion model. The distribution of anomaly parameters α (upper panel) shows an apparent shift to the normal diffusion by knocking out lamin A protein. The distribution of the dwell time τ_Γ (lower panel) obtained from all measured cells represents a longer time to leave the observed volume in absence of lamin A protein. (b) Using 2-component normal diffusion model we extracted the distribution of slow diffusion coefficient D_{slow} (upper panel) and the fraction of slow component ρ_{slow} (lower panel). The bound histones are evidently more dominant in the absence of lamin A. A statistical summary of the fit results is reported in Table 3.2.

3.3 Dynamic spatial rearrangement of chromatin

Rearrangement of chromatin structure, as a result of the depletion of lamin A , can be recognised through spatial correlation analysis of the image series. For this reason, utilising Eq. 2.49, auto-correlation function and the spatial fluorescence cross-correlation between each single $1 * 1$ pixel and its neighbouring 5 pixels was calculated (spanning up to 2000 nm vicinity of the reference pixels), assuming there had been no flow throughout the data acquisition ($\|\vec{v}\| = 0$).
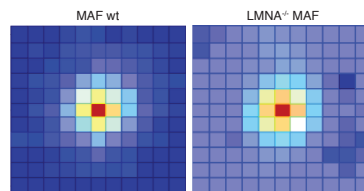
Figure 3.8: 2D colour maps of spatial cross-correlation amplitude normalised by auto-correlation amplitude for a representative MAF and LMNA$^{-/-}$ MAF. The colours are arranged in the form of heat map from dark blue denoting 0 (no correlation) to bright red (autocorrelation)

Appropriate $1 * 1$ pixel masking based on intensity thresholds and the visible periphery of the nucleus for each cell had been done manually before the correlation, to avoid computing cross-correlation with

dark single pixels. From the resulting cross-correlation functions, the amplitude of function at $\tau = 0$ was extracted and normalised by the zero-lag autocorrelation amplitude and then averaged for all unmasked pixels. Figure 3.8 displays a 2D colormap matrices, in which the central square is the average value of all the autocorrelation functions calculated at each unmasked $1 * 1$ pixel and each neighbouring square represents the average value of spatial cross correlation amplitude at that pixel distance. It is evident that higher correlations at longer spatial range can be tracked in the knockout cell. This result indicates a looser arrangement of chromatin in the absence of nucleoplasmic lamins, whereas in the wildtype cell, a more localised motion of histones is more probable. This can be explained by a possible crosslinking functions of A-type lamins.

Additionally, radial average of the normalised cross-correlation values at each given distance was considered for better quantification. This procedure has been applied to the data from 26 cells (13 MAFs and 13 LMNA$^{-/-}$ MAFs) , imaged on different days to have a better statistics. In Figure 3.9 the mean value of radial averages calculated from these cells is plotted against the distance. The faster decay of spatial cross-correlation amplitude can be better recognised in this plot.
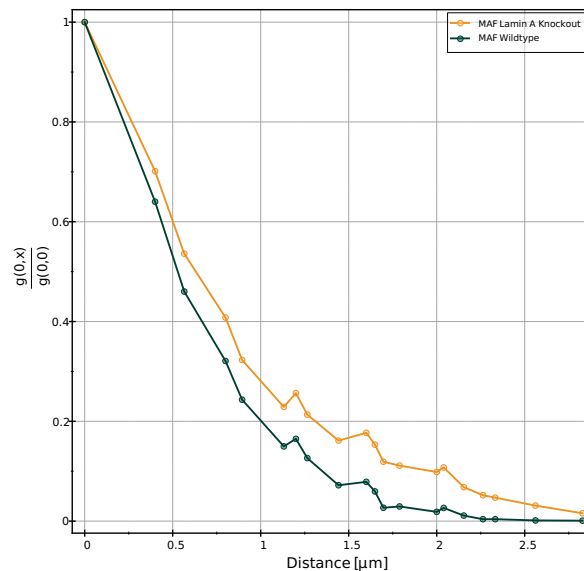
Figure 3.9: Mean value of radial averages calculated from amplitude of cross-correlation functions for MAF cells and LMNA$^{-/-}$ MAF cells. Each data point for a cell line shows the mean value of radial averages at the given distance over 13 cells.

The same spatial cross-correlation analysis scheme was performed on the imaging data of 100 nm fluorescent microspheres diffusing in agarose gels of different concentrations to study the effect of viscoelasticity on the spatial cross-correlation of diffusing particles. Figure 3.10 shows a comparison between the 2D colormaps and indicates higher spatial co-mobility in denser systems compared to water. Figure 3.11 summarises this results for around 25 sample bags for each concentration of agarose gels.

On the first glance, this result seemed to contradict our findings in the cells. But it can be an evidence that nucleoplasmic A-type lamins are not polymerising in the interior of the nucleus and instead they are interacting with chromatin and other nuclear bodies. Therefore, the heterogenous gel like environment might no be disrupted by their absence.
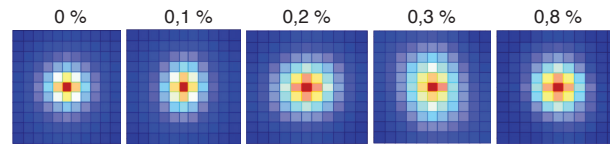
Figure 3.10: 2D colour maps of spatial cross-correlation amplitude normalised by auto-correlation amplitude for different concentrations of agarose gels. The colours are arranged in the form of heat map from dark blue denoting 0 (no correlation) to bright red (autocorrelation).
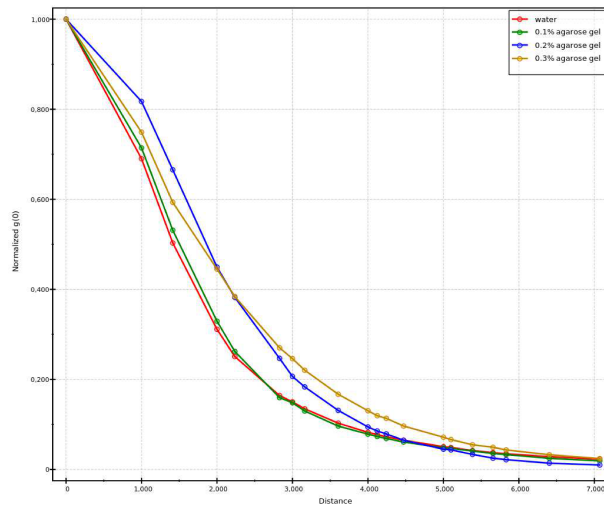
Figure 3.11: Mean value of cross correlation ampltitude radial averages for different concentrations of agarose gels. Each data point shows the mean value of radial averages at the given distance over around 25 sample bags.

4 Langevin dynamics simulation

4.1 The description of the model

To study polymer-nanoparticle mixtures, comparable to the case of chromatin in nucleoplasmic A-type lamin pool, by computer simulation, both Monte-Carlo and molecular dynamics approaches were conducted before. Crucial ingredients such as polymer compressibility, confinement and viscoelastic effects on polymer looping were included in these simulations to deliver results, applicable to realistic situations.

Our simulation framework to describe chromatin-lamins interconnection is based on a Langevin dynamics model of a flexible polymer consisting of n monomers of diameter σ, in which each monomer is interacting with direct neighbour through a nonlinear spring modelled by a finitely extensible nonlinear elastic (FENE) potential,

$$U_{\text{FENE}}(r) = -\frac{k}{2}\, r_{\text{max}}^2 \log\left(1 - r^2/r_{\text{max}}^2\right), \tag{4.1}$$

where, k is the spring constant, r_{max} is the maximum allowed separation between two monomers and r is the distance between them. Excluded-volume interactions between polymer segments are given by a standard truncated Lennard-Jones repulsive potential (Weeks-Chandler-Anderson potential [119])

$$U_{\text{LJ}}(r, \epsilon) = \begin{cases} 4\epsilon\left(\left(\sigma/r_{i,j}\right)^{12} - \left(\sigma/r_{i,j}\right)^6\right) + \epsilon & r_{i,j} < r_{\text{cut}} \\ 0 & \text{otherwise} \end{cases} \tag{4.2}$$

with $r_{\text{cut}} = 2^{1/6}\sigma$. In this equation, $r_{i,j} = |r_i - r_j|$ is the inter-monomer distance, σ is the the diameter of a chain monomer and ϵ is the strength of the potential. We measure the length in units of σ and the energy in units of thermal energy $k_B T$, in which k_B is the Boltzmann constant and T is the absolute temperature. The parameters for these two potentials are set to $k = 30$, $r_{\text{max}} = 1.5$ (to minimise bond crossings of the chain), $\epsilon = 1$ and $\sigma = 1$.

The bending energy of the chain is given by

$$U_b = \frac{\kappa}{2}\sum_{i=2}^{n-1}\theta_i^2, \tag{4.3}$$

here, κ is the bending stiffness and θ_i is the bending angle of the ith chain segment. The persistence length of the chain for a given value of κ is then $l_p = {}^{2\kappa l_0^3}/_{k_b T}$ in two-dimensions. κ is set to 3 for a close approximation of the persistence length of chromatin. The dynamics of the position $r_i(t)$ of the chain monomer then is governed by the following overdamped Langevin equation

$$m\frac{d^2 r_i}{dt^2} = -\nabla\left(\sum_{j=1, j\neq i}^{n} U_{LJ}(|r_i - r_j|) + U_{\text{FENE}}(|r_i - r_{i\pm 1}|) + U_b(r_i)\right) + \eta_i(t), \tag{4.4}$$

here m is the mass of the monomer, $\eta_i(t)$ is the white Gaussian noise with unit variance at each direction, $\langle \eta_i(t)\cdot\eta_j(t')\rangle = 6k_B T\delta_{ij}\delta(t-t')$, where δ_{ij} is the Kronecker symbol. This relation is satisfying the fluctuation-dissipation theorem. For solving the Eq. 4.4 numerically, the stochastic Runge-Kutta algorithm [120] was

implemented together utilising a Verlet list for the optimisation. The integration time step was set to $\Delta t = 10^{-4}$ to maintain the convergence of the numerical solver. Initially the system is equilibrated for $\sim 10^6$ steps and run up to $\sim 10^8$ steps. The desired quantities such as the number of loops and the radius of gyration are evaluated at each 10^4 steps after the equilibration of the chain.

On the presumption that A-type lamins are binding to chromatin and rendering the loop formation energetically profitable, another attractive potential is considered as well.This complies with the most speculated role of nucleoplasmic lamin As as crosslinkers. The potential is defined via another LJ potential with a larger cutoff distance and attraction strength ϵ_s, called the pairing energy

$$U_{\text{att}}(r) = U_{LJ}(r, \epsilon_s) + C_{\text{LJ}}, \tag{4.5}$$

The constant C_{LJ} is introduced along so that the attraction potential becomes continuous at $r = r_{\text{cutoff}}$ with the zero-value branch of Eq. 4.2 at $r > r_{\text{cutoff}}$. This attraction potential acts when the distance between two given monomers is less than a critical distance characterised by the size of a lamin A protein $\sim 664\text{aa}$. The self-avoidance of chain monomers vanishes between the immediate neighbours of the two monomers that are attracted to each other, for the loops to be formed effectively.

For this simulation, a polymer chain of 128 monomers was taken into account and the initial pairing energy set to $\epsilon_s = 20\epsilon \equiv 20k_BT$. We varied this paring energy $0 \leq \epsilon_s \leq 1600k_BT$ to examine the effect of the pairing strength on the dynamics of the polymer chain. Figure 4.1 shows a snapshot of a simulated polymer undergoing Langevin dynamics in the presence of looping agents after equilibration.
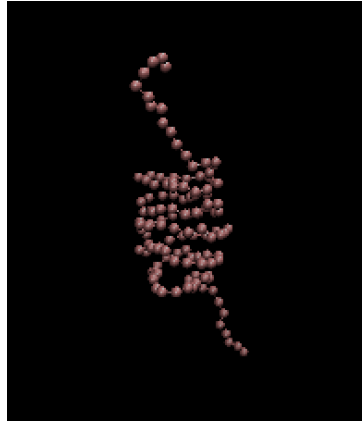
Figure 4.1: A snapshot, generated from the simulation showing a polymer chain in its compact conformation. The spheres are monomers connected by nonlinear springs

4.2 Loop formation and diffusion

First the diffusive motion of a polymer chain without the binding agents was considered. For this reason the time-averaged MSD (tMSD) of the centre of the mass (COM) of the polymer was calculated from the chain trajectory generated at each time step

$$\text{tMSD}(\tau) = \overline{\delta_X^2(\tau)} = \frac{1}{T-\tau} \int_0^{T-\tau} (X(t+\tau) - X(t))^2 \, dt, \tag{4.6}$$
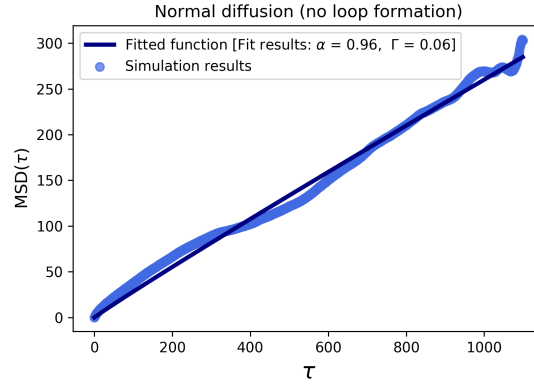
Figure 4.2: Mean squared displacement in the absence of the loop forming agents. The thicker more transparent line illustrate the simulation data and the brighter thiner line the fit model. Simulation parameters: $\epsilon_s = 0$, $\sigma = 1$, $\kappa = 3$.

where

$$X(t) = \frac{1}{n} \sum_{i=1}^{n} x_i \tag{4.7}$$

is the COM of the polymer. Moreover, the tMSD is averaged over an ensemble of all independent traces of each monomer during the time of the simulation

$$\text{nMSD}(\tau) = \overline{\langle \delta_X^2(\tau) \rangle} = \frac{1}{N} \sum_{i=1}^{n} \overline{\delta_X^2(\tau)} \tag{4.8}$$

Then a power-law model for anomalous diffusion Eq. 2.42 was fitted to the resulting $nMSD$ data. Figure 4.2 shows that the anomaly exponent is almost equal to one $\alpha = 0.96$, indicating a normal diffusion. This result is in line with our findings on the diffusion pattern in lamin A depleted cell line.
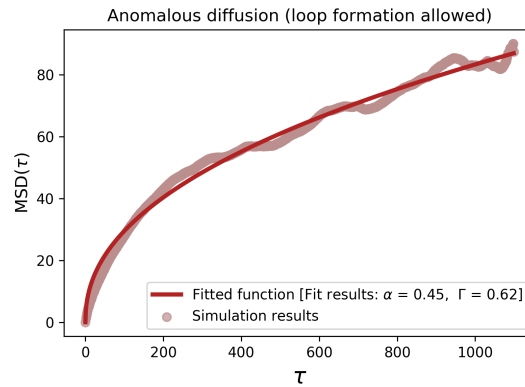
Figure 4.3: Mean squared displacement in the presence of the loop forming agents. The thicker more transparent line illustrate the simulation data and the brighter thiner line the fit model. Simulation parameters: $\epsilon_s = 800 k_B T$, $\sigma = 1$, $\kappa = 3$.

The same treatment has been applied to the data from the simulation in which loop formation was allowed. The resulting plot for the case of $\epsilon_s = 800 k_B T$ is sketched in Figure 4.3 representing a clear hinderance in the motion of chromatin.

Note that no other frictional forces was taken into account in our model, therefore it is possible to deduce that formation of loops alone can render anomaly in the system. This suggests that lamins can be involved in packing of DNA in the nucleoplasm and therefore they affect the arrangement of chromatin. More rigorous analysis of parameters are needed for a more conclusive picture. But these results provides a footing for further investigation on this regard.

Chromatin folding

To study the internal confinement of chromatin due to crowding, static quantities such as radius of gyration are often considered. It can characterise the size of the polymers of any structure which can be greatly beneficial for studying a dynamic polymer chain. The squared radius of gyration R_g^2 is defined as the average squared distance between monomers in a given conformation and the polymer COM

$$R_g^2 = \frac{1}{N} \sum_{i=1}^{N} (r_i - r_j)^2. \tag{4.9}$$

The value for radius of gyration at each 10^4 step was recorded for different values of pairing energy. The results are summarised in Figure 4.4. As it is seen in this figure, with increase in the pairing energy the mean value of gyration radii decreases, implying more compact spatial arrangement of the chromatin. A broad distribution of gyration radii can be seen from the violinplot (Figure 4.4(a)) at weak paring strengths, however at $2\epsilon_s$ already a drop is recognisable. At $\epsilon > 100k_BT$ the radii significantly shift to shorter r values and at high strength. It is almost fluctuating around its mean.
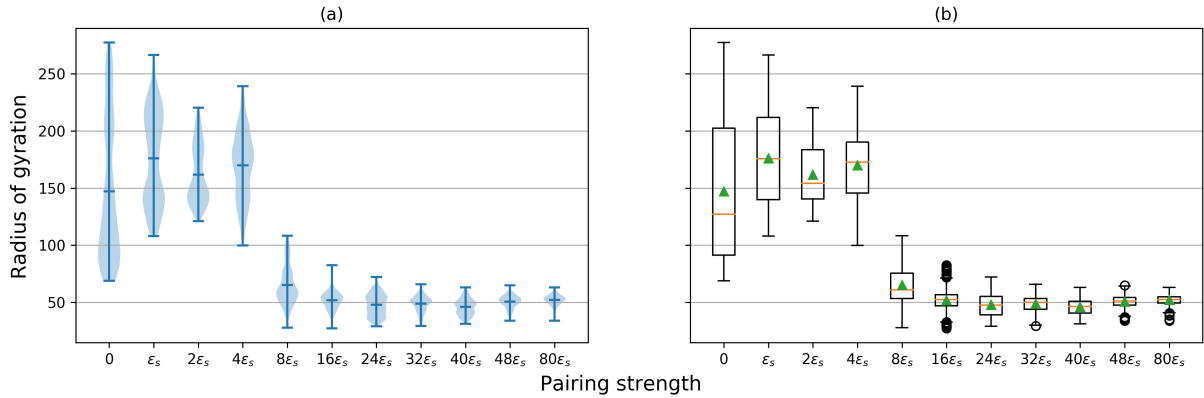
Figure 4.4: A statistical overview of radii of gyration for different pairing strengths. (a) displays the distribution of gyration radii at each pairing strength. In (b) a detailed boxplot of this quantity is presented. the green triangles denote the mean value of radii at each pairing strength and the horizontal line denotes the median. Simulation parameters: $\sigma = 1$, $\kappa = 3$.

These results are in a good compliance with our findings presented in Section 3.3 (Dynamic spatial rearrangement of chromatin) as it predicts the loose arrangement of polymers in the absence of crosslinkers.

DISCUSSION

5 Conclusion and outlook

5.1 Restatement of the problem

The function of the genome in the cell depends strongly on its three-dimensional structure and dynamics [121, 122]. Chromatin in the cell nucleus is highly ordered yet dynamic. The principles of its organization, crucial for proper cell function, still remain unclear [123, 124]. Here, to get further insight into these mechanisms, we focused on the effect of lamin A on chromatin dynamics.

Evidence is growing that nuclear lamins form a filamentous scaffold throughout the nucleus, which not only determines its shape and mechanical properties, but also serves as a docking site for chromatin and for many proteins that participate in chromatin organization[118]. Besides the extensive lamin structures located within the nuclear lamina, smaller and more dynamic lamin polymers may form protein complexes involved in a wide range of nuclear housekeeping functions such as DNA replication, DNA repair[125–130] and RNA pol II transcription[131]. More specifically, single particle tracking of telomers in live cells indicated that knockout of lamin A strikingly alters the dynamics, inducing a transition from anomalous diffusion to normal diffusion. However, the depletion of LAP2α, a protein that interacts with lamin A and chromatin, has no effect on the anomaly of diffusion [118, 132]. This suggested the prominent role of lamin A mediated interconnections in chromatin in controlling its dynamics.

Dynamics of chromatin and proteins in the cell nucleus have been visualized by modern light microscopy techniques. To characterize chromatin dynamics in live cells, we use fluorescence correlation and cross-correlation spectroscopy in a single plane illumination microscope (SPIM-FCS/FCCS) to achieve parallel acquisition of FCS data across entire lines or regions [101, 133]. FCS yields mobility parameters through an auto-correlation analysis of fluorescence fluctuations measured inside a small observation volume. SPIM-FCS allows such an auto-correlation analysis on fast image series for hundreds of thousands of contiguous pixels, thereby providing 2-dimensional mobility and interaction maps in live cells [95]. Two-color cross-correlation (FCCS) in addition provides information about the interactions and co-mobility between differently labelled particles and 2-focus cross-correlation produces data on spatial arrangement of a polymer network and the viscoelasticity of its surrounding environment. This method has been utilised successfully before as an example, it has been shown that the mobility of a heterodimeric transcription factor strongly correlated with the degree of dimerization, spatially localizing specific binding to DNA in the dimer form exploiting SPIM-FC(C)S [104, 134, 135].

5.2 Summary of our findings

We applied SPIM-FC(S)S to study the influence of lamin A on the mobility of chromatin fluorescently labelled with H2A-eGFP. Earlier experimental studies on transport processes inside the cells has demonstrated that the intranuclear diffusion of particles is anomalous[21, 55, 136–138]. This is likely due to macromolecular crowding and/or viscoelasticity of the nuclear micro-environment, that hinder the random motions of particles. There are different polymer models to describe these anomalous dynamics. Guigas et al. studied the diffusion of gold nanospheres in cells and found out that their anomalous diffusion is in agreement with Rouse model for polymer dymanics [21]. This indicates that the intranuclear environment resembles a polymeric sponge. However, Erdel et al. have shown that a more detailed model, namely porous medium model, is needed to explain the subdiffusivity of chromatin. They summarised different polymer models and deduced that a porous medium or random obstacle network for diffusing particles can better characterise the interior of the nucleus [139]. Brownian dynamics simulations also showed that the chromatin chain alone would not display anomalous diffusion; this requires in addition

the presence of a viscoelastic matrix around the polymer [138]. We show that the diffusion anomaly parameter α of chromatin-bound histones in mouse adult fibroblasts is $\alpha = 0.83 \pm 0.08$, indicating this subdiffusion. This is in a good compliance with the results presented in Erdel et al. [139]. In a lamin A knockout cell line, on the other hand, diffusion reverted to normal ($\alpha = 1.11 \pm 0.10$), but significantly slowed down. This change in chromatin dynamics suggests that the lamin network is the source of the nucleoplasmic viscoelasticity. In the absence of lamin A, the nucleoplasm loses its viscoelastic behavior, reducing diffusion obstruction. Furthermore, the loss of the elastic lamin A interconnections reduces the overall speed of chromatin motion, as indicated by the longer residence time in the focal volume. This can be also seen from the two-component model since the fraction of slowly diffusing histones in lamin A knockout cells increases. This agrees with theoretical predictions which showed that the loop closure time for an elastic polymer chain is accelerated by viscoelasticity [140–143]. It is noteworthy that our findings agree with recent findings by Garini's group on telomere motion in the cells lacking lamin A proteins [118].

To understand better how lamin A affects the viscoelasticity of the nuclear interior, we analyzed the diffusion of an inert probe, eGFP tetramer((eGFP)-4x), with the same technique. In lamin A deficient cells, the mobility of free eGFP-4x is significantly slowed down (from $D_{fast} = 17.9 \pm 2.2 \ \mu m^2/s$ in the wildtype cells to $D_{fast} = 12.1 \pm 1.8 \ \mu m^2/s$ in the knockout ones). This result supports the view that lamin A is responsible for the viscoelasticity of the nuclear interior.

We also examine the interactions between lamin A and chromatin, performing SPIM-FCCS measurements on mouse cells where lamins and histones are labelled with different colors. The significant cross-correlation amplitude (Figure 3.1) demonstrates that a relatively large fraction of lamin A is moving together with histones. Since the decay time of the cross-correlation curves is comparable with the dwell time of histones bound to chromatin, we can infer that lamin A and chromatin are co-diffusing.

Our spatial cross-correlation analysis of the data provided more insight on the spatial rearrangement of chromatin after the depletion nucleoplasmic A-type lamins. Our studies demonstrate a more flexible chromatin configuration and a looser positioning in the entire nucleus. This effect can be seen from higher correlation values at longer spatial range. The same procedure applied to artificial system of diffusing microspheres in gels showed the influence of viscoelastic dense network on the cross-correlation amplitude. The loss of this spatial correlation in supposedly more crowded environment containing nucleoplasmic lamins, hence, can be explained by their dynamic tendency to interconnect with chromatin fibre, possibly as crosslinkers, as opposed to forming homo-dimers. This results can be improved by an optical system with a better spatial resolution to probe the effect more accurately at defined distances.

A Langevin dynamics simulation on a polymer chain in three-dimensional model system has been employed as a framework to mimic these interconnections. Different scenarios for the nature of the interaction between nucleoplasmic lamin A and chromatin can be explored by these simulations. Here, assuming that their bindings facilitates the polymer looping as suggested in [142], we managed to show the extreme compaction of the polymer chain in the presence of these loop forming agents. A change in the MSD of its constituting monomers, in addition, is an indicator of anomaly inducing effects of crosslinkers in our model system. Both results are in line with our experimental findings on the chromatin and lamin A interdependence.

5.3 Future outlook

As it is implied throughout this thesis, SPIM-FC(C)S provides a robust and reliable platform to study the dynamics of macromolecules in viscoelastic media. One of the limitations of our system though, was its time resolution. Employing faster detectors to reach μs resolutions for data acquisition will therefore considerably enhance the system to study faster dynamics of smaller molecules. Moreover, it can offer a possibility to explore the complex dynamics of diffusion in a system to validate theoretical speculations
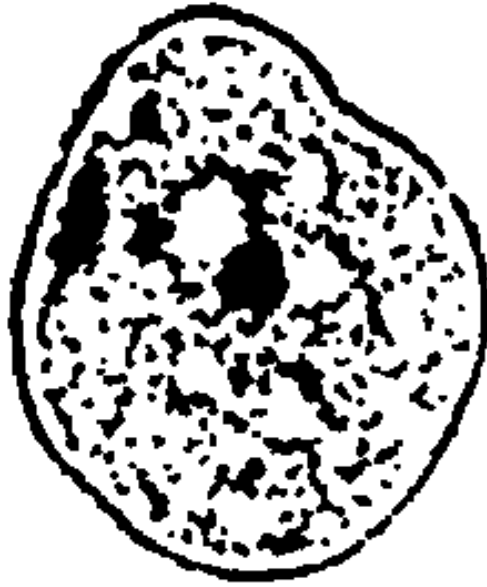
Figure 5.1: An inverted black and white STED image of the nucleus of a MAF, smoothed and processed. Chromatin fibre is present in black regions and white regions represent the interchromatin space.

in shorter time ranges. On the other hand, new achievements in super resolution microscopy techniques, termed as nanoscopy, provides a better spatial resolution at macromolecular scales. Combining one of the methods called super-resolution stimulated emission depletion (STED) [144], with fluorescence correlation spectroscopy has already shown promising results [145–147]. These enhancement can be complimentary to SPIM-FC(C)S which will results in better profiling of dynamics both in time and space and ultimately lead to much better quantification of underlying physical parameters of the system.

Studying the fluctuations in complex system has become an active field of research in theoretical physics, especially in last two decades. The emergence of new theories on the nature of these fluctuations allows us to gain better insight on the properties of the system. This together with new experimental discoveries dictate a systematic modelling approach to examine their possible implications in real life. As an example relevant to the scope of this thesis, new view on chromatin as a highly variable structure suggests that chromatin is less physically constrained and more dynamic than expected in the regular static structure model [68]. This can be explained and studied by considering the complex nature of the dynamics in short time scales manifested in anomalous non Gaussian behaviour of the parameters. The need to incorporate the realistic physical parameters and proper system scaling would therefore provides meaningful results in future. This can be done by applying different types of diffusion model other than the ones assumed throughout this thesis, both in the simulation framework and in the fit models. Altering the parameters of the simulation such as the bending rigidity of the polymer either in time or based on its interactions with other constituent of the system to build a more dynamic system can be suggested as a new path to investigate in future.

Lastly, we need to acquire more relevant structural information on nuclear intermediate filaments in living cells. Therefore employing novel image processing methods on static nanoscopic fluorescent images can be beneficial. The image shown in Figure 5.1 is the result of our recent attempt on determining the interchromatin domains in the nucleus of a MAF cell by STED imaging. It gives us more information on

the arrangement of chromatin in an interphase nucleus. A simple study by image segmentation based on the intensity profiles of this image and another image taken from LMNA$^-$ MAF yields interesting information on chromatin conformation in the nucleus. Furthermore, a two-color STED image is able to elucidate the positioning of nucleoplasmic A-type lamins with respect to chromatin fibre, which can be later exploited both by modifying the simulation model and in space-time correlation analysis of dynamic image series with lower spatial resolutions to ultimately unravel the function of these nucleoplasmic intermediate filaments.

Publication

The following article was published in the course of my doctoral studies.

[54]   Fereydoon Taheri et al. 'Random Motion of Chromatin Is Influenced by Lamin A Interconnections'.
In: *Biophys. J.* 114.10 (May 2018), pp. 2465–2472. DOI: 10.1016/j.bpj.2018.04.037 (cited on pages 6, 9).

Bibliography

Here are the references in citation order.

[1]   Ralf Metzler and Joseph Klafter. 'The random walk's guide to anomalous diffusion: a fractional dynamics approach'. In: *Phys. Rep.* 339.1 (Dec. 2000), pp. 1–77. DOI: 10.1016/S0370-1573(00)00070-3 (cited on pages 2, 4, 5).

[2]   R Brown. 'A brief Account of Microscopical Observation made in Months of June, July and August, 1827, on the Particles contained in the Pollen of Plants'. In: *Philos. Mag. Ann. Philos. [New Ser.* 4(21).21 (1829), pp. 161–173 (cited on page 2).

[3]   M. D. Haw. *Colloidal suspensions, brownian motion, molecular reality: A short history.* 2002. DOI: 10.1088/0953-8984/14/33/315 (cited on page 2).

[4]   Mary Jo Nye. *Molecular Reality: a perspective on the scientific work of Jean Perrrin.* First edit. Elsevier Publishing Company, 1972 (cited on page 2).

[5]   Albert Einstein. 'On the Motion of Small Particles Suspended in a Stationary Liquid'. In: *Ann. Phys.* 322 (1905), pp. 549–560. DOI: 10.1002/andp.19053220806 (cited on page 2).

[6]   Fernando A. Oliveira et al. 'Anomalous Diffusion: A Basic Mechanism for the Evolution of Inhomogeneous Systems'. In: *Front. Phys.* 7 (Feb. 2019), p. 18. DOI: 10.3389/fphy.2019.00018 (cited on page 2).

[7]   L. Bachelier. 'Théorie de la spéculation'. In: *Ann. Sci. l'École Norm. supérieure* 17 (1900), pp. 21–86. DOI: 10.24033/asens.476 (cited on page 3).

[8]   Jean Philibert. 'One and a Half Century of Diffusion: Fick, Einstein, before and beyond'. In: *Diffus. Fundam. Leipzig 2005.* Ed. by Jörg Kärger. Leipziger Universitätsverlag, 2005, 2005. Chap. 1, pp. 8–17 (cited on page 3).

[9]   jean Perrin and Jean Perrin Mouvement brownien. 'Mouvement brownien et grandeurs moléculaires'. In: *Le Radium* 6.12 (Dec. 1909), pp. 353–360 (cited on page 3).

[10] Debashish Chowdhury. '100 years of Einstein's theory of Brownian motion: from pollen grains to protein trains'. In: (Apr. 2005) (cited on page 4).

[11] Ralf Metzler and Joseph Klafter. *From stretched exponential to inverse power-law: fractional dynamics, Cole-Cole relaxation processes, and beyond.* Tech. rep. 2002, pp. 81–87 (cited on pages 4, 5).

[12] James Clerk Maxwell. 'On the Dynamical Theory of Gases'. In: *Philos. Trans. R. Soc. London* 157 (Jan. 1867), pp. 49–88. DOI: 10.1017/cbo9780511710377.003 (cited on page 4).

[13] Peter Debye. *Polar molecules.* New York: The Chemical Catalog Company Inc., 1929 (cited on page 4).

[14] Nigel Goldenfeld and Leo P. Kadanoff. *Simple lessons from complexity.* Apr. 1999. DOI: 10.1126/science.284.5411.87 (cited on pages 4, 9).

[15] L. Peliti and A. Vulpiani, eds. *Measures of Complexity.* Vol. 314. Lecture Notes in Physics. Berlin, Heidelberg: Springer Berlin Heidelberg, 1988 (cited on page 4).

[16] B. V. (Boris Vladimirovich) Gnedenko and A. N. (Andreĭ Nikolaevich) Kolmogorov. *Limit distributions for sums of independent random variables.* Addison-Wesley, 1954 (cited on page 5).

[17] B. D. (Barry D.) Hughes. *Random walks and random environments.* Clarendon Press, 1995 (cited on page 5).

[18] Paul Lévy. *Calcul des probabilités.* Paris : Gauthier-Villars, 1925 (cited on page 5).

[19] Paul Lévy. 'Théorie de l'addition des variables aléatoires'. In: (1937) (cited on page 5).

[20] Bruce J. West and William Deering. 'Fractal physiology for physicists: Lévy statistics'. In: *Phys. Rep.* 246.1-2 (Oct. 1994), pp. 1–100. DOI: 10.1016/0370-1573(94)00055-7 (cited on page 5).

[21] Gernot Guigas and Matthias Weiss. 'Sampling the Cell with Anomalous Diffusion?The Discovery of Slowness'. In: *Biophys. J.* 94.1 (2008), pp. 90–94. DOI: https://doi.org/10.1529/biophysj.107.117044 (cited on pages 5, 6, 40).

[22] L Hufnagel, D Brockmann, and T Geisel. 'Forecast and control of epidemics in a globalized world'. In: *Proc. Natl. Acad. Sci. U. S. A.* 101.42 (2004), pp. 15124–15129. DOI: 10.1073/pnas.0308344101 (cited on page 5).

[23] Benoit Palmieri et al. 'Multiple scale model for cell migration in monolayers: Elastic mismatch between cells enhances motility'. In: *Sci. Rep.* 5.1 (Dec. 2015), p. 11745. DOI: 10.1038/srep11745 (cited on page 5).

[24] Diana Goldstein et al. 'Origin of active transport in breast-cancer cells'. In: *Soft Matter* 9.29 (July 2013), pp. 7167–7173. DOI: 10.1039/c3sm50172h (cited on page 5).

[25] Samudrajit Thapa et al. 'Transient superdiffusion of polydisperse vacuoles in highly motile amoeboid cells'. In: *J. Chem. Phys.* 150.14 (Apr. 2019), p. 144901. DOI: 10.1063/1.5086269 (cited on page 5).

[26] Oleg V. Bychuk and Ben O'Shaughnessy. 'Anomalous diffusion at liquid surfaces'. In: *Phys. Rev. Lett.* 74.10 (Mar. 1995), pp. 1795–1798. DOI: 10.1103/PhysRevLett.74.1795 (cited on page 5).

[27] R. Balescu. 'Anomalous transport in turbulent plasmas and continuous time random walks'. In: *Phys. Rev. E* (1995). DOI: 10.1103/PhysRevE.51.4807 (cited on page 5).

[28] Marta C González, César A Hidalgo, and Albert László Barabási. 'Understanding individual human mobility patterns'. In: *Nature* 453.7196 (2008), pp. 779–782. DOI: 10.1038/nature06958 (cited on page 5).

[29] G. M. Viswanathan et al. 'Lévy flight search patterns of wandering albatrosses'. In: *Nature* 381.6581 (May 1996), pp. 413–415. DOI: 10.1038/381413a0 (cited on page 5).

[30] G. M. Viswanathan et al. 'Optimizing the success of random searches'. In: *Nature* 401.6756 (Oct. 1999), pp. 911–914. DOI: 10.1038/44831 (cited on page 5).

[31] Gabriel Ramos-Fernández et al. 'Lévy walk patterns in the foraging movements of spider monkeys (Ateles geoffroyi)'. In: *Behav. Ecol. Sociobiol.* 55.3 (Jan. 2004), pp. 223–230. DOI: 10.1007/s00265-003-0700-6 (cited on page 5).

[32] Denner S. Vieira et al. 'Anomalous diffusion behavior in parliamentary presence'. In: *Phys. Rev. E* 99.4 (Apr. 2019), p. 042141. DOI: 10.1103/PhysRevE.99.042141 (cited on page 5).

[33] Lin Guo et al. 'Heterogeneous and anomalous diffusion inside lipid tubules'. In: *J. Phys. Chem. B* 111.51 (2007), pp. 14244–14249. DOI: 10.1021/jp076562n (cited on page 5).

[34] L. F. Richardson. 'Atmospheric Diffusion Shown on a Distance-Neighbour Graph'. In: *Proc. R. Soc. A Math. Phys. Eng. Sci.* 110.756 (Apr. 1926), pp. 709–737. DOI: 10.1098/rspa.1926.0043 (cited on page 5).

[35] Ralf Metzler and Joseph Klafter. 'The restaurant at the end of the random walk: recent developments in the description of anomalous transport by fractional dynamics'. In: *J. Phys. A. Math. Gen.* 37.31 (2004), R161. DOI: 10.1088/0305-4470/37/31/R01 (cited on page 5).

[36] Harvey Scher and Elliott W. Montroll. 'Anomalous transit-time dispersion in amorphous solids'. In: *Phys. Rev. B* 12.6 (Sept. 1975), pp. 2455–2477. DOI: 10.1103/PhysRevB.12.2455 (cited on page 5).

[37] J Čermák and I Stloukal. 'Diffusion and structural changes in Fe 91 y Mo 8 Cu 1 B y alloys'. In: *J. Phys. Condens. Matter* 19.15 (Apr. 2007), p. 156219. DOI: 10.1088/0953-8984/19/15/156219 (cited on pages 5, 6).

[38] G. Pfister and H. Scher. 'Time-dependent electrical transport in amorphous solids: As2Se3'. In: *Phys. Rev. B* 15.4 (Feb. 1977), pp. 2062–2083. DOI: 10.1103/PhysRevB.15.2062 (cited on page 5).

[39] G. Pfister and H. Scher. 'Dispersive (non-Gaussian) transient transport in disordered solids'. In: *Adv. Phys.* 27.5 (Sept. 1978), pp. 747–798. DOI: 10.1080/00018737800101474 (cited on page 5).

[40] G. Zumofen, A. Blumen, and J. Klafter. 'Current flow under anomalous-diffusion conditions: Lévy walks'. In: *Phys. Rev. A* 41.8 (Apr. 1990), pp. 4558–4561. DOI: 10.1103/PhysRevA.41.4558 (cited on page 5).

[41] Qing Gu et al. 'Non-Gaussian transport measurements and the Einstein relation in amorphous silicon'. In: *Phys. Rev. Lett.* 76.17 (Apr. 1996), pp. 3196–3199. DOI: 10.1103/PhysRevLett.76.3196 (cited on pages 5, 6).

[42] P. W.M. Blom and M. C.J.M. Vissenberg. 'Dispersive hole transport in poly(p-phenylene vinylene)'. In: *Phys. Rev. Lett.* 80.17 (Apr. 1998), pp. 3819–3822. DOI: 10.1103/PhysRevLett.80.3819 (cited on pages 5, 6).

[43] Harvey Scher, Michael F. Shlesinger, and John T. Bendler. 'Time-Scale Invariance in Transport and Relaxation'. In: *Phys. Today* 44.1 (Jan. 1991), pp. 26–34. DOI: 10.1063/1.881289 (cited on pages 5, 6).

[44] Yuh Fukai and H. Sugimoto. 'Hydrogen Diffusion in Metals - Unsolved Problems'. In: *Defect Diffus. Forum* 83 (Jan. 1992), pp. 87–110. DOI: 10.4028/www.scientific.net/ddf.83.87 (cited on page 6).

[45] Aleksander Stanislavsky and Karina Weron. 'Transport of magnetic bright points on the Sun. Analysis of subdiffusion scenarios'. In: *Astrophys. Space Sci.* 323.4 (Oct. 2009), pp. 351–355. DOI: 10.1007/s10509-009-0083-x (cited on page 6).

[46] A. Shalchi. 'Time-dependent transport and subdiffusion of cosmic rays'. In: *J. Geophys. Res. Sp. Phys.* 110.A9 (Sept. 2005). DOI: 10.1029/2005JA011214 (cited on page 6).

[47] A. A. Lagutin and V. V. Uchaikin. 'Anomalous diffusion equation: Application to cosmic ray transport'. In: *Nucl. Instruments Methods Phys. Res. Sect. B Beam Interact. with Mater. Atoms.* Vol. 201. 1. North-Holland, Jan. 2003, pp. 212–216. DOI: 10.1016/S0168-583X(02)01362-9 (cited on page 6).

[48] J. Kota and J. R. Jokipii. 'Velocity Correlation and the Spatial Diffusion Coefficients of Cosmic Rays: Compound Diffusion'. In: *Astrophys. J.* 531.2 (Mar. 2000), pp. 1067–1070. DOI: 10.1086/308492 (cited on page 6).

[49] F Amblard et al. 'Subdiffusion and anomalous local viscoelasticity in actin networks'. In: *Phys. Rev. Lett.* 77.21 (1996), pp. 4470–4473. DOI: 10.1103/PhysRevLett.77.4470 (cited on page 6).

[50] Nicolas Fatin-Rouge, Konstantin Starchev, and Jacques Buffle. 'Size Effects on Diffusion Processes within Agarose Gels'. In: *Biophys. J.* 86.5 (May 2004), pp. 2710–2719. DOI: 10.1016/S0006-3495(04)74325-8 (cited on page 6).

[51] Daniel S. Banks and Cécile Fradin. 'Anomalous diffusion of proteins due to molecular crowding'. In: *Biophys. J.* 89.5 (Nov. 2005), pp. 2960–2971. DOI: 10.1529/biophysj.104.051078 (cited on page 6).

[52] Matthias Weiss, Hitoshi Hashimoto, and Tommy Nilsson. 'Anomalous protein diffusion in living cells as seen by fluorescence correlation spectroscopy'. In: *Biophys. J.* 84.6 (June 2003), pp. 4043–4052. DOI: 10.1016/S0006-3495(03)75130-3 (cited on page 6).

[53] Matthias Weiss and Tommy Nilsson. 'In a mirror dimly: tracing the movements of molecules in living cells'. In: *Trends Cell Biol.* 14.5 (May 2004), pp. 267–273. DOI: 10.1016/J.TCB.2004.03.012 (cited on page 6).

[54] Fereydoon Taheri et al. 'Random Motion of Chromatin Is Influenced by Lamin A Interconnections'. In: *Biophys. J.* 114.10 (May 2018), pp. 2465–2472. DOI: 10.1016/j.bpj.2018.04.037 (cited on pages 6, 9).

[55] Felix Höfling and Thomas Franosch. 'Anomalous transport in the crowded world of biological cells'. In: *Reports Prog. Phys.* 76.4 (Apr. 2013), p. 46602. DOI: 10.1088/0034-4885/76/4/046602 (cited on pages 6, 40).

[56] Ron Milo et al. 'BioNumbers The database of key numbers in molecular and cell biology'. In: *Nucleic Acids Res.* 38.SUPPL.1 (Jan. 2009), pp. D750–3. DOI: 10.1093/nar/gkp889 (cited on page 6).

[57] Naama Gal, Diana Lechtman-Goldstein, and Daphne Weihs. *Particle tracking in living cells: A review of the mean square displacement method and beyond*. 2013. DOI: 10.1007/s00397-013-0694-6 (cited on pages 6, 7).

[58] Benjamin M Regner et al. 'Anomalous diffusion of single particles in cytoplasm'. In: *Biophys. J.* 104.8 (2013), pp. 1652–1660. DOI: 10.1016/j.bpj.2013.01.049 (cited on page 6).

[59] Ohad Medalia et al. 'Macromolecular architecture in eukaryotic cells visualized by cryoelectron tomography'. In: *Science (80-.).* 298.5596 (Nov. 2002), pp. 1209–1213. DOI: 10.1126/science.1076184 (cited on page 6).

[60] Dan N. Simon and Katherine L. Wilson. *The nucleoskeleton as a genome-associated dynamic 'network of networks'*. Nov. 2011. DOI: 10.1038/nrm3207 (cited on pages 7, 8).

[61] Larry Gerace, Andrea Blum, and Günter Blobel. 'Immunocytochemical localization of the major polypeptides of the nuclear pore complex-lamina fraction: Interphase and mitotic distribution'. In: *J. Cell Biol.* 79.2 (Nov. 1978), pp. 546–566. DOI: 10.1083/jcb.79.2.546 (cited on pages 7, 8).

[62] Kris Noel Dahl et al. 'The nuclear envelope lamina network has elasticity and a compressibility limit suggestive of a molecular shock absorber'. In: *J. Cell Sci.* 117.20 (Oct. 2004), pp. 4779–4786. DOI: 10.1242/jcs.01357 (cited on page 7).

[63] Farshid Guilak, John R. Tedrow, and Rainer Burgkart. 'Viscoelastic properties of the cell nucleus'. In: *Biochem. Biophys. Res. Commun.* 269.3 (Mar. 2000), pp. 781–786. DOI: 10.1006/bbrc.2000.2360 (cited on page 7).

[64] Pavel Hozák et al. 'Visualization of replication factories attached to a nucleoskeleton'. In: *Cell* 73.2 (Apr. 1993), pp. 361–373. DOI: 10.1016/0092-8674(93)90235-I (cited on page 7).

[65] Stephen T Spagnol, Travis J Armiger, and Kris Noel Dahl. 'Mechanobiology of Chromatin and the Nuclear Interior'. In: *Cell. Mol. Bioeng.* 9.2 (June 2016), pp. 268–276. DOI: 10.1007/s12195-016-0444-9 (cited on pages 7, 8).

[66] Michael R. Hübner and David L. Spector. 'Chromatin Dynamics'. In: *Annu. Rev. Biophys.* 39.1 (Apr. 2010), pp. 471–489. DOI: 10.1146/annurev.biophys.093008.131348 (cited on pages 7, 8).

[67] Tom Misteli. *Beyond the Sequence: Cellular Organization of Genome Function*. Feb. 2007. DOI: 10.1016/j.cell.2007.01.028 (cited on pages 7, 8).

[68] Kazuhiro Maeshima, Satoru Ide, and Michael Babokhov. *Dynamic chromatin organization without the 30-nm fiber*. June 2019. DOI: 10.1016/j.ceb.2019.02.003 (cited on pages 7, 42).

[69] Benjamin Albert et al. *Nuclear organization and chromatin dynamics in yeast: Biophysical models or biologically driven interactions?* June 2012. DOI: 10.1016/j.bbagrm.2011.12.010 (cited on page 8).

[70] Tom Misteli. *Concepts in nuclear architecture*. May 2005. DOI: 10.1002/bies.20226 (cited on page 8).

[71] Stanislaw A Gorski, Miroslav Dundr, and Tom Misteli. *The road much traveled: trafficking in the cell nucleus*. June 2006. DOI: 10.1016/j.ceb.2006.03.002 (cited on page 8).

[72] Sofia A Quinodoz et al. 'Higher-Order Inter-chromosomal Hubs Shape 3D Genome Organization in the Nucleus'. In: *Cell* 174.3 (2018), 744–757.e24. DOI: 10.1016/j.cell.2018.05.024 (cited on page 8).

[73] Thomas Cremer et al. *Chromosome territories - a functional nuclear landscape*. June 2006. DOI: 10.1016/j.ceb.2006.04.007 (cited on page 8).

[74] Howard J Worman, Cecilia Ostlund, and Yuexia Wang. 'Diseases of the nuclear envelope.' In: *Cold Spring Harb. Perspect. Biol.* 2.2 (Feb. 2010), a000760. DOI: 10.1101/cshperspect.a000760 (cited on page 8).

[75] Nolwenn Briand et al. *Lamin A, chromatin and FPLD2: Not just a peripheral Ménage-à-Trois*. July 2018. DOI: 10.3389/fcell.2018.00073 (cited on page 8).

[76] Travis A Dittmer and Tom Misteli. 'The lamin protein family.' In: *Genome Biol.* 12.5 (May 2011), p. 222. DOI: 10.1186/gb-2011-12-5-222 (cited on pages 8, 9).

[77] R. P. Aaronson and G. Blobel. 'Isolation of nuclear pore complexes in association with a lamina'. In: *Proc. Natl. Acad. Sci. U. S. A.* 72.3 (Mar. 1975), pp. 1007–1011. DOI: 10.1073/pnas.72.3.1007 (cited on page 8).

[78] Frank D. Mckeon, Marc W. Kirschner, and Daniel Caput. 'Homologies in both primary and secondary structure between nuclear envelope and intermediate filament proteins'. In: *Nature* 319.6053 (Feb. 1986), pp. 463–468. DOI: 10.1038/319463a0 (cited on page 8).

[79] D. Z. Fisher, N. Chaudhary, and G. Blobel. 'cDNA sequencing of nuclear lamins A and C reveals primary and secondary structural homology to intermediate filament proteins'. In: *Proc. Natl. Acad. Sci. U. S. A.* 83.17 (Sept. 1986), pp. 6450–6454. DOI: 10.1073/pnas.83.17.6450 (cited on page 8).

[80] F Lin and H J Worman. 'Structural organization of the human gene encoding nuclear lamin A and nuclear lamin C.' In: *J. Biol. Chem.* 268.22 (Aug. 1993), pp. 16321–6 (cited on page 8).

[81] Feng Lin and Howard J. Worman. 'Structural organization of the human gene (LMNB1) encoding nuclear lamin B1'. In: *Genomics* 27.2 (May 1995), pp. 230–236. DOI: 10.1006/geno.1995.1036 (cited on page 8).

[82] Brian Burke and Colin L. Stewart. *The nuclear lamins: Flexibility in function.* Jan. 2013. DOI: 10.1038/nrm3488 (cited on page 9).

[83] Rebecca de Leeuw, Yosef Gruenbaum, and Ohad Medalia. *Nuclear Lamins: Thin Filaments with Major Functions.* Jan. 2018. DOI: 10.1016/j.tcb.2017.08.004 (cited on page 9).

[84] Qian Ye and Howard J. Worman. 'Protein-protein interactions between human nuclear lamins expressed in yeast'. In: *Exp. Cell Res.* 219.1 (July 1995), pp. 292–298. DOI: 10.1006/excr.1995.1230 (cited on page 9).

[85] T Dechat et al. 'Lamina-associated polypeptide 2alpha binds intranuclear A-type lamins.' In: *J. Cell Sci.* 113 Pt 19 (Oct. 2000), pp. 3473–84 (cited on page 9).

[86] J M Bridger et al. 'Internal lamin structures within G1 nuclei of human dermal fibroblasts.' In: *J. Cell Sci.* 104 (Pt 2 (Feb. 1993), pp. 297–306 (cited on page 9).

[87] B K Kennedy et al. 'Nuclear organization of DNA replication in primary mammalian cells.' In: *Genes Dev.* 14.22 (Nov. 2000), pp. 2855–68. DOI: 10.1101/gad.842600 (cited on page 9).

[88] Nana Naetar et al. 'Loss of nucleoplasmic LAP2α-lamin A complexes causes erythroid and epidermal progenitor hyperproliferation'. In: *Nat. Cell Biol.* 10.11 (Nov. 2008), pp. 1341–1348. DOI: 10.1038/ncb1793 (cited on page 9).

[89] Takeshi Shimi et al. 'The A- and B-type nuclear lamin networks: Microdomains involved in chromatin organization and transcription'. In: *Genes Dev.* 22.24 (Dec. 2008), pp. 3409–3421. DOI: 10.1101/gad.1735208 (cited on page 9).

[90] Jos L.V. Broers et al. 'Dynamics of the nuclear lamina as monitored by GFP-tagged A-type lamins'. In: *J. Cell Sci.* 112.20 (Oct. 1999), pp. 3463–3475 (cited on page 9).

[91] Robert D. Moir et al. 'Nuclear lamins A and B1: Different pathways of assembly during nuclear envelope formation in living cells'. In: *J. Cell Biol.* 151.6 (Dec. 2000), pp. 1155–1168. DOI: 10.1083/jcb.151.6.1155 (cited on page 9).

[92] Yagmur Turgay et al. 'The molecular architecture of lamins in somatic cells'. In: *Nature* 543.7644 (Mar. 2017), pp. 261–264. DOI: 10.1038/nature21382 (cited on page 9).

[93] Douglas Magde, Elliot Elson, and W. W. Webb. 'Thermodynamic fluctuations in a reacting system measurement by fluorescence correlation spectroscopy'. In: *Phys. Rev. Lett.* 29.11 (Sept. 1972), pp. 705–708. DOI: 10.1103/PhysRevLett.29.705 (cited on page 10).

[94] Oleg Krichevsky and Grégoire Bonnet. 'Fluorescence correlation spectroscopy: The technique and its applications'. In: *Reports Prog. Phys.* 65.2 (Feb. 2002), pp. 251–297. DOI: 10.1088/0034-4885/65/2/203 (cited on page 10).

[95] Jan Wolfgang Krieger et al. 'Dual-color fluorescence cross-correlation spectroscopy on a single plane illumination microscope (SPIM-FCCS)'. In: *Opt Express* 22.3 (Feb. 2014), pp. 2358–2375. DOI: 10.1364/OE.22.002358 (cited on pages 10, 12–14, 17–20, 22, 23, 40).

[96] R. Rigler et al. 'Fluorescence correlation spectroscopy with high count rate and low background: analysis of translational diffusion'. In: *Eur. Biophys. J.* 22.3 (Aug. 1993), pp. 169–175. DOI: 10.1007/BF00185777 (cited on page 10).

[97] M Eigen and R Rigler. *Sorting single molecules: Application to diagnostics and evolutionary biotechnology.* June 1994. DOI: 10.1073/pnas.91.13.5740 (cited on page 10).

[98] K. M. Berland. *Fluorescence correlation spectroscopy: new methods for detecting molecular associations.* Apr. 1997. DOI: 10.1016/S0006-3495(97)78796-4 (cited on page 10).

[99] Manfred Auer et al. *Fluorescence correlation spectroscopy: Lead discovery by miniaturized HTS.* Oct. 1999. DOI: 10.1016/S1359-6446(98)01240-9 (cited on page 10).

[100] Jagadish Sankaran et al. 'ImFCS: A software for Imaging FCS data analysis and visualization'. In: *Opt. Express* 18.25 (Dec. 2010), p. 25468. DOI: 10.1364/oe.18.025468 (cited on page 10).

[101] Thorsten Wohland et al. 'Single Plane Illumination Fluorescence Correlation Spectroscopy (SPIM-FCS) probes inhomogeneous three-dimensional environments'. In: *Opt. Express* 18.10 (May 2010), p. 10627. DOI: 10.1364/oe.18.010627 (cited on pages 10, 13, 40).

[102] Jagadish Sankaran et al. 'Accuracy and precision in camera-based fluorescence correlation spectroscopy measurements'. In: *Anal. Chem.* 85.8 (Apr. 2013), pp. 3948–3954. DOI: 10.1021/ac303485t (cited on pages 10, 16).

[103] Anand Pratap Singh et al. 'The performance of 2D array detectors for light sheet based fluorescence correlation spectroscopy'. In: *Opt. Express* 21.7 (Apr. 2013), p. 8652. DOI: 10.1364/oe.21.008652 (cited on pages 10, 13).

[104] A Pernus et al. 'Imaging Fos-Jun transcription factor mobility and interaction in live cells by single plane illumination-fluorescence cross correlation spectroscopy'. In: *PLoS One* 10.4 (Apr. 2015). Ed. by Jinxing Lin, e0123070. DOI: 10.1371/journal.pone.0123070 (cited on pages 10, 40).

[105] M. Born and E. Wolf. *Principles of Optics 7th edition.* 1999 (cited on page 12).

[106] Paul Hopkins et al. 'The van Hove distribution function for Brownian hard spheres: Dynamical test particle theory and computer simulations for bulk dynamics'. In: *J. Chem. Phys.* 133.22 (Dec. 2010), p. 224505. DOI: 10.1063/1.3511719 (cited on page 16).

[107] L. A. Pipes and Mary L. Boas. 'Mathematical Methods in the Physical Sciences.' In: *Am. Math. Mon.* 74.8 (1967), p. 1024. DOI: 10.2307/2315314 (cited on page 16).

[108] Tomasz Wocjan et al. 'Dynamics of a fluorophore attached to superhelical DNA: FCS experiments simulated by Brownian dynamics'. In: *Phys. Chem. Chem. Phys.* 11.45 (Nov. 2009), pp. 10671–10681. DOI: 10.1039/b911857h (cited on page 19).

[109] Roman Shusterman et al. 'Monomer Dynamics in Double- and Single-Stranded DNA Polymers'. In: *Phys. Rev. Lett.* 92.4 (Jan. 2004), p. 4. DOI: 10.1103/PhysRevLett.92.048303 (cited on page 19).

[110] Roman Shusterman, Tatyana Gavrinyov, and Oleg Krichevsky. 'Internal dynamics of superhelical DNA'. In: *Phys. Rev. Lett.* 100.9 (Mar. 2008), p. 098102. DOI: 10.1103/PhysRevLett.100.098102 (cited on page 19).

[111] E. P. Petrov et al. 'Diffusion and segmental dynamics of double-stranded DNA'. In: *Phys. Rev. Lett.* 97.25 (Dec. 2006), p. 258101. DOI: 10.1103/PhysRevLett.97.258101 (cited on page 19).

[112] Jan W Krieger et al. 'Imaging fluorescence (cross-) correlation spectroscopy in live cells and organisms'. In: *Nat. Protoc.* 10.12 (Dec. 2015), pp. 1948–1974. DOI: 10.1038/nprot.2015.100 (cited on page 19).

[113] Talley J. Lambert. *FPbase: a community-editable fluorescent protein database.* Apr. 2019. DOI: 10.1038/s41592-019-0352-8 (cited on page 23).

[114] Nana Naetar, Simona Ferraioli, and Roland Foisner. *Lamins in the nuclear interior - Life outside the lamina*. 2017. DOI: 10.1242/jcs.203430 (cited on page 26).

[115] Teresa Sullivan et al. 'Loss of A-type lamin expression compromises nuclear envelope integrity leading to muscular dystrophy'. In: *J. Cell Biol.* 147.5 (Nov. 1999), pp. 913–919. DOI: 10.1083/jcb.147.5.913 (cited on page 26).

[116] N Dross et al. 'Mapping eGFP oligomer mobility in living cell nuclei'. In: *PLoS One* 4.4 (2009), e5041. DOI: 10.1371/journal.pone.0005041 (cited on page 31).

[117] György Vámosi et al. 'EGFP oligomers as natural fluorescence and hydrodynamic standards'. In: *Sci. Rep.* 6 (Sept. 2016), 33022 EP –- (cited on page 31).

[118] I. Bronshtein et al. 'Loss of lamin A function increases chromatin dynamics in the nuclear interior'. In: *Nat. Commun.* 6.1 (Dec. 2015), p. 8044. DOI: 10.1038/ncomms9044 (cited on pages 31, 40, 41).

[119] John D. Weeks, David Chandler, and Hans C. Andersen. 'Role of repulsive forces in determining the equilibrium structure of simple liquids'. In: *J. Chem. Phys.* 54.12 (June 1971), pp. 5237–5247. DOI: 10.1063/1.1674820 (cited on page 35).

[120] Rebecca L. Honeycutt. 'Stochastic Runge-Kutta algorithms. I. White noise'. In: *Phys. Rev. A* 45.2 (Jan. 1992), pp. 600–603. DOI: 10.1103/PhysRevA.45.600 (cited on page 35).

[121] R Paul et al. 'Propagation of mechanical stress through the actin cytoskeleton toward focal adhesions: model and experiment'. In: *Biophys J* 94.4 (2008), pp. 1470–1482. DOI: 10.1529/biophysj.107.108688 (cited on page 40).

[122] N Wang, J D Tytell, and D E Ingber. 'Mechanotransduction at a distance: mechanically coupling the extracellular matrix with the nucleus'. In: *Nat Rev Mol Cell Biol* 10.1 (2009), pp. 75–82. DOI: 10.1038/nrm2594 (cited on page 40).

[123] Peter Fraser and Wendy Bickmore. *Nuclear organization of the genome and the potential for gene regulation*. May 2007. DOI: 10.1038/nature05916 (cited on page 40).

[124] Malte Wachsmuth, Mawen Caudron-Herger, and Karsten Rippe. 'Genome organization: Balancing stability and plasticity'. In: *Biochim. Biophys. Acta - Mol. Cell Res.* 1783.11 (2008), pp. 2061–2079. DOI: https://doi.org/10.1016/j.bbamcr.2008.07.022 (cited on page 40).

[125] Ian Gibbs-Seymour et al. 'Lamin A/C-dependent interaction with 53BP1 promotes cellular responses to DNA damage'. In: *Aging Cell* 14.2 (Apr. 2015), pp. 162–169. DOI: 10.1111/acel.12258 (cited on page 40).

[126] Robert Mahen et al. 'A-Type Lamins Maintain the Positional Stability of DNA Damage Repair Foci in Mammalian Nuclei'. In: *PLoS One* 8.5 (2013), pp. 1–9. DOI: 10.1371/journal.pone.0061893 (cited on page 40).

[127] Susana Gonzalo. 'DNA Damage and Lamins'. In: *Cancer Biol. Nucl. Envel. Recent Adv. May Elucidate Past Parad.* Ed. by Eric C Schirmer and Jose I de las Heras. New York, NY: Springer New York, 2014, pp. 377–399. DOI: 10.1007/978-1-4899-8032-8_17 (cited on page 40).

[128] Joe Swift et al. 'Nuclear Lamin-A Scales with Tissue Stiffness and Enhances Matrix-Directed Differentiation'. In: *Science (80-.).* 341.6149 (Aug. 2013), p. 1240104. DOI: 10.1126/science.1240104 (cited on page 40).

[129] Jerome Irianto et al. 'Nuclear lamins in cancer'. In: *Cell Mol Bioeng* 9.2 (June 2016), pp. 258–267. DOI: 10.1007/s12195-016-0437-8 (cited on page 40).

[130] Sangkyun Cho, Jerome Irianto, and Dennis E Discher. 'Mechanosensing by the nucleus: From pathways to scaling relationships'. In: *J Cell Biol* 216.2 (Feb. 2017), pp. 305–315. DOI: 10.1083/jcb.201610042 (cited on page 40).

[131] Yehuda Brody et al. 'The In Vivo Kinetics of RNA Polymerase II Elongation during Co-Transcriptional Splicing'. In: *PLOS Biol.* 9.1 (2011), pp. 1–18. DOI: 10.1371/journal.pbio.1000573 (cited on page 40).

[132] Anat Vivante et al. 'Genome organization in the nucleus: From dynamic measurements to a functional model'. In: *Methods* 123 (July 2017), pp. 128–137. DOI: https://doi.org/10.1016/j.ymeth.2017.01.008 (cited on page 40).

[133] Jérémie Capoulade et al. 'Quantitative fluorescence imaging of protein diffusion and interaction in living cells'. In: *Nat Biotechnol* 29.9 (Aug. 2011), pp. 835–839. DOI: 10.1038/nbt.1928 (cited on page 40).

[134] Peter Brazda et al. 'Ligand Binding Shifts Highly Mobile Retinoid X Receptor to the Chromatin-Bound State in a Coactivator-Dependent Manner, as Revealed by Single-Cell Imaging'. In: *Mol. Cell. Biol.* 34.7 (2014), pp. 1234–1245. DOI: 10.1128/MCB.01097-13 (cited on page 40).

[135] Nikoletta Szalóki et al. 'Evidence for Homodimerization of the c-Fos Transcription Factor in Live Cells Revealed by Fluorescence Microscopy and Computer Modeling'. In: *Mol Cell Biol* 35.21 (Nov. 2015), pp. 3785–3798. DOI: 10.1128/MCB.00346-15 (cited on page 40).

[136] Malte Wachsmuth, Waldemar Waldeck, and Jörg Langowski. 'Anomalous diffusion of fluorescent probes inside living cell investigated by spatially-resolved fluorescence correlation spectroscopy'. In: *J. Mol. Biol.* 298.4 (2000), pp. 677–689. DOI: 10.1006/jmbi.2000.3692 (cited on page 40).

[137] Matthias Weiss et al. 'Anomalous Subdiffusion Is a Measure for Cytoplasmic Crowding in Living Cells'. In: *Biophys. J.* 87.5 (Nov. 2004), pp. 3518–3524. DOI: https://doi.org/10.1529/biophysj.104.044263 (cited on page 40).

[138] C C Fritsch and J Langowski. 'Chromosome dynamics, molecular crowding, and diffusion in the interphase cell nucleus: a Monte Carlo lattice simulation study'. In: *Chromosom. Res* 19.1 (2011), pp. 63–81. DOI: 10.1007/s10577-010-9168-1 (cited on pages 40, 41).

[139] Fabian Erdel, Michael Baum, and Karsten Rippe. 'The viscoelastic properties of chromatin and the nucleoplasm revealed by scale-dependent protein mobility'. In: *J. Phys. Condens. Matter* 27.6 (2015), p. 64115 (cited on pages 40, 41).

[140] Rajarshi Chakrabarti. 'Dynamics of end-to-end loop formation for an isolated chain in viscoelastic fluid'. In: *Phys. A Stat. Mech. its Appl.* 391.22 (2012), pp. 5326–5331. DOI: http://dx.doi.org/10.1016/j.physa.2012.06.025 (cited on page 41).

[141] Jaeoh Shin, Andrey G. Cherstvy, and Ralf Metzler. 'Kinetics of polymer looping with macro-molecular crowding: Effects of volume fraction and crowder size'. In: *Soft Matter* 11.3 (Dec. 2015), pp. 472–488. DOI: 10.1039/c4sm02007c (cited on page 41).

[142] Jaeoh Shin et al. 'Facilitation of polymer looping and giant polymer diffusivity in crowded solutions of active particles'. In: *New J. Phys.* 17.11 (Oct. 2015), p. 113008. DOI: 10.1088/1367-2630/17/11/113008 (cited on page 41).

[143] Jaeoh Shin and Anatoly B. Kolomeisky. 'Facilitation of DNA loop formation by protein-DNA non-specific interactions'. In: (Jan. 2019) (cited on page 41).

[144] Stefan W. Hell and Jan Wichmann. 'Breaking the diffraction resolution limit by stimulated emission: stimulated-emission-depletion fluorescence microscopy'. In: *Opt. Lett.* 19.11 (June 1994), p. 780. DOI: 10.1364/ol.19.000780 (cited on page 42).

[145] Alf Honigmann et al. 'Scanning STED-FcS reveals spatiotemporal heterogeneity of lipid interaction in the plasma membrane of living cells'. In: *Nat. Commun.* 5.1 (Dec. 2014), p. 5412. DOI: 10.1038/ncomms6412 (cited on page 42).

[146] Erdinc Sezgin et al. 'Measuring nanoscale diffusion dynamics in cellular membranes with super-resolution STED–FCS'. In: *Nat. Protoc.* 14.4 (Apr. 2019), pp. 1054–1083. DOI: 10.1038/s41596-019-0127-9 (cited on page 42).

[147] Aurélien Barbotin et al. 'Adaptive optics allows STED-FCS measurements in the cytoplasm of living cells'. In: *Opt. Express* 27.16 (Aug. 2019), p. 23378. DOI: 10.1364/oe.27.023378 (cited on page 42).